Winter 12-17-2021

The Development of a Novel Blood-Brain Barrier, Organ-on-a-Chip System and the Identification of Erythrocytes as a Key Contributor to Age-Associated Neurological Decline

Payam Amiri
Keck Graduate Institute

The Development of a Novel Blood-Brain Barrier, Organ-on-a-Chip System and the Identification of Erythrocytes as a Key Contributor to Age-Associated Neurological Decline

By Payam Amiri, M.B.S.

A dissertation submitted to the Henry E. Riggs School of Applied Life Sciences, Keck Graduate Institute in partial fulfillment of the requirements for the degree of Doctor of Philosophy in Applied Life Sciences

Claremont, California

2021

Approved by:

Kiana Aran, Ph.D.

Associate Professor of Medical Diagnostics and Therapeutics

Doctoral Thesis Advisor

KGI KECK GRADUATE INSTITUTE

OFFICE OF THE REGISTRAR

PhD Dissertation Completion Form

We, the undersigned, certify that we have read this dissertation of Payam Amiri 972030263

Name and ID#

and approve it as adequate in scope and quality for the degree of Doctor of Philosophy.

Dissertation Committee:

Kiana Aran	Kiana Aran	Digitally signed by Kiana Aran Date: 2021.12.05 21:13:03 -08'00'
(Typed name of Chair), Chair	*Signature*	
Rachita Sumbria	Rachita Sumbria	Digitally signed by Rachita Sumbria Date: 2021.12.03 15:54:40 -08'00'
(Typed name), Member	*Signature*	
Irina Conboy	Irina M. Conboy	Digitally signed by Irina M. Conboy Date: 2021.12.06 08:52:05 -08'00'
(Typed name), Member	*Signature*	
(Typed name), Visiting Examiner	*Signature*	
James D. Sterling	James D. Sterling	Digitally signed by James D. Sterling Date: 2021.12.09 14:57:33 -08'00'
(Typed name), PhD Program Director	*Signature*	

Abstract

The Impact of Blood Components on Aging

Payam Amiri, Kiana Aran (PI)

Advancements in modern medicine have greatly extended human life expectancy. However, with the onset of age-associated conditions such as Alzheimer's disease, autoimmune disorders, and certain cancers, healthy aging is becoming an increasingly pressing issue. Blood exchanges between young and old partners demonstrate old blood can cause detrimental effect to the young animal, notably on the brain tissue. However, the complexity of blood makes it difficult to identify what role the individual factors play in the aggregate observed effect. This dissertation seeks to explore the potential effects of erythrocytes on the brain as we age. Erythrocyte morphology and rigidity changes as mammals age, altering their physical dynamics as they flow within the capillary bed. This impacts downstream biological events, such as the release of reactive oxygen species and hemoglobin, potentially compromising the blood-brain barrier. This work outlines the development of the next generation of blood exchange tools to further understand the role of blood in aging. Additionally, this work aims to develop a novel blood-brain barrier, organ-on-a-chip and to test the impact of erythrocytes on the brain. In doing so, we identify erythrocytes as a critical contributor to age-associated neurological decline.

Dedication

I dedicate this work to my mom and dad. It is because of their decades of selflessness and sacrifice that I have arrived to where I am today. Mom, every personal or career move you have ever made was with only myself and my sister in mind. Dad, you dedicated yourself to ensure that your children would have luxuries that you did not have growing up. You both were younger than I am now when you fled Iran to seek greater opportunities, and you both are braver than I could ever imagine to be. I was able to succeed because the two of you put me on the path to success.

Acknowledgments

This work could not have been completed had it not been for the incredible support network of colleges, friends, and family that have supported me in this journey. For the sake of brevity, I cannot name everyone that aided me in this journey, but there are some notable individuals that I would like to highlight.

My amazing mother Shahpar Amiri, father Djavad Amiri, and sister Dalia Amiri have supported me and have helped me grow from a wide-eyed kid, excited about the world, into the person I am today. I could not have completed this work without the opportunities the three of you have provided me, and the council you all provided me has guided me through my challenging ordeals.

My loving girlfriend and partner, Natalie Chan. You have seen me through my Ph.D. journey from its very beginning. Having you in my corner has pushed me beyond what I thought were my limits. Thank you for your patience all those nights when I would stay late in the lab. Thank you for supporting me when I felt like I was drowning under a sea of work. Thank you for always lending a hand when I needed one. Thank you for being my confidant and for always knowing what to say. You've been absolutely amazing and I could not have undertaken this journey without you.

My closest friends, Shane Kubow, Thanh Tran, and Justin Kubow. I could always count on you guys to pick me up or provide me an escape. Even though you guys have been hundreds of miles away, I always felt like you guys were right by my side.

To my furry buds Zoey the cat and Moose the corgi. Zoey, you've been with me for years, and you have always seemed to know when I needed you the most. Moose,

seeing you grow up has been my single greatest experience through the COVID-19 pandemic. Even though you two do not get along currently, I still have not given up hope that you will get there eventually.

I would like to thank my colleges and mentors who I have learned so much from. Josh Littig, Jonalyn DeCastro, Sarah Balderston, Ritwik Keshav, Tra-Thanh Tran, Melod Mehdipour, Jhaline Mast, Chaerim Kang, Victor Mora, Dr. Hsiang-Wei Lu, Dr. Reza Hajian, Dr. Regis Peytavi, Dr. Alexander Kane, Dr. Brett Goldsmith, and Dr. Michael Conboy.

Thank you to the members of my committee and previous supervisors, Dr. Irina Conboy, Dr. Rachita Sumbria, Dr. Animesh Ray, and Dr. Heidi Moralez. I thank you all, for the opportunity to grow under your supervision and for all that you have taught me.

And lastly, I would like to warmly thank Dr. Kiana Aran. Thank you for welcoming me into your lab and for taking a chance on me. Thank you for always challenging me and presenting me with opportunities to learn. You have always wanted nothing but success for me and you have pushed me further than I would have ever thought that I could go. You have guided me to develop as a scientist, a professional, and as a person. I am a completely different person than who I was when we first met, and I am confident that my time with you has placed me on a trajectory for success.

Table of Contents

Acknowledgments…… IV

Table of Contents VI

Table of Abbreviations IX

Chapter 1: Introduction and Scope of Thesis 1

Chapter 2: The Development of Blood Exchange Tools..... 11

Chapter 3: The Development of the First-Generation Blood-Brain Barrier Organ on a Chip..... 29

Chapter 4: The Development of the Second-Generation Blood-Brain Barrier Organ on a Chip, Micro Electrical Blood-Brain Barrier (µE-BBB..... 40

Chapter 5. The Identification of Erythrocytes as a Contributor to Age-Associated Loss of Blood-Brain Barrier Integrity..... 55

Thesis Conclusion..... 74

References 78

Table of Abbreviations

A	Ampere
ABS	Acrylonitrile Butadiene Styrene
AC	Alternating Current
BBB	Blood-Brain Barrier
bEnd.3	Mouse Brain Endothelial Cell Line
C8-D1A	Mouse Astrocyte Type-I Cell Line
CAD	Computer-Aided Design
CLDN-5	Claudin-5
CNS	Central Nervous System
DC	Direct Current
DMEM	Dulbecco's Modified Eagle Medium
DPI	Diphenyleneiodonium
eNOS	Endothelial Nitric Oxide Synthase
eNOSi	Endothelial Nitric Oxide Synthase Inhibitor
EtOH	Ethanol
EVOM	Endothelial Volt-Ohm Meter
FITC	Fluorescein Isothiocyanate
GFAP	Glial Fibrillary Acidic Protein
Hb	Hemoglobin
ICC	Immunocytochemistry
IPA	Isopropanol
µE-BBB	Micro Electrical Blood-Brain Barrier

NO	Nitric Oxide
PBS	Phosphate Buffered Saline
PC	Polycarbonate
PE	Polyethylene
PFA	Paraformaldehyde
SEM	Standard Error of Mean
SNAP	S-Nitroso-N-Acetylpenicillamine
TEER	Tran Endothelial Electrical Resistance
TGF-β	Transforming Growth Factor-Beta
TJ	Tight Junctions
V	Volt
W	Watt
ZO-1	Zonula Occludens-1

Table of Figures

Figure 1.1: Blood exchange between young and old partners have demonstrated to have rejuvenative effects on blood exchange young and old partners.[1]

Figure 1.2: Following blood exchange between young and old mice, there was a significant decline in the young animal's hippocampal neurogenesis, but there was no observed improvement in the neurogenesis of the old animal.[1]

Figure 1.3: The BBB is composed of various cells, including endothelial astrocyte and pericyte cells. This structure separates the animal's circulating blood from the CNS.[2]

Figure 1.4: The erythrocyte membrane deforms to a paraboloid shape to better accommodate the shear stress in the capillary beds. Here, the black arrows depict the flow profile of shear stress forces. Erythrocytes from old animals (bottom) cannot deform as readily as young animal erythrocytes (top), due to their greater rigidity, and retain their discus shape.[3]

Figure 2.1: The single pump microfluidic blood handling system is a 3D printed device that features a single pump head.

Figure 2.2: The dual pump microfluidic blood handling system is a 3D printed device that features 2 independent pump heads.

Figure 2.3: The 3D printed components of the single pump were designed to interact with a section of silicone tubing with a 22g inlet and outlet. The 22g connectors can connect to polyethylene-50 tubing, or 3 French polyurethane tubing.

Figure 2.4: The 3D printed components of the dual pump were designed to interact with a section of silicone tubing with a 22g inlet and outlet per pump head. The 22g connectors can connect to polyethylene-50 tubing, or 3 French polyurethane tubing.

Figure 2.5: The pump rollers were fabricated from a section of 22g hypodermic tubing, nested within a 18g bushing. The free rotating bushing can make contact with the silicone tubing of the system without fraying or excessively damaging the silicone material.

Figure 2.6: The wiring diagram of the single pump system allows for the single stepper motor to be controlled by the Arduino Uno through the motor driver.

Figure 2.7: The wiring diagram of the dual pump system allows for the 2 stepper motors to be controlled by the Arduino Uno through the Adafruit motor shield.

Figure 2.8: The code for the single pump is directed by 4 variables, that the user may adjust to calibrate the system or modify the parameters for the desired experiment.

Figure 2.9: To only use a single pump from the dual pump, 4 variables are used to control the system that the user may adjust to calibrate the system or modify the parameters for the desired experiment. The specific pump may also be selected.

Figure 2.10: To only use both pumps from the dual pump, 4 variables are used to control the system that the user may adjust to calibrate the system or modify the parameters for the desired experiment.

Figure 2.11: Back-and-forth simulation exchanges were conducted between mice of different or similar sizes, and the percent exchanged was compared to a mathematical model.

Figure 2.12: Extraction-replacement simulation exchanges were conducted between a simulated mouse and a stock of simulated blood, and the percent exchanged was compared to a mathematical model.

Figure 2.13: To execute an in vivo blood exchange, a mouse needs to be connected to the blood handling system via a surgically placed jugular vein catheter.

Figure 3.1: The BBB organ-on-a-chip device is composed of three layers. The endothelial cells may be able to grow within the culture wells of the device and interact with erythrocytes that are perfused through the channels in the upper layer. The cells grown within the device will grow over interdigitated electrodes.

Figure 3.2: The interdigitated electrodes are featured on a standard glass slide. Each electrode set is composed of two independent electrodes that form a comb-like structure. The off-set electrodes can be used to monitor the electrical resistance of a cell culture monolayer.

Figure 3.3: The culture-only device consists of a single PDMS layer bound to glass. The PDMS contains features that serve as culture well and the purpose of this device is to optimize cell culture methodologies.

Figure 3.4: The culture-channel device is a combination of the PDMS cell culture well structures of the previous device with the PDMS thin channel structures. The device does not contain the TEER interdigitated electrodes and the cells in this device are grown on PDMS. The purpose of this device is to optimize experimental protocols.

Figure 3.5: After 5 days of culture, the endothelial cells have become fully confluent and adopted a striated conformation. The cells are confined to the growth region and do not grow past the PDMS wall on the upper right corner of the figure.

Figure 3.6: The bEnd.3 cells grown within the culture-only device were stained for ZO-1 (green) and costained with DRAQ5 (red) after 5 days of growth. By this point, the cells are highly confluent and are strongly expressing the ZO-1 TJ marker at the cell-to-cell junction, indicating a positive stain.

Figure 4.1: The μE-BBB consists of a lumen and basolateral chamber with integrated TEER electrodes. The chambers are separated by a porous PC membrane. The two compartments of the device allow for endothelial and astrocyte cells to grow in close

proximity to each other. The barrier may be monitored through TEER measurements and through the paracellular leakage of molecules across the simulated BBB. Figure was adapted with permission from Biorender.com under a paid academic subscription.[3]

Figure 4.2: Traditional TEER electrodes do not form a uniform electric field between terminals. An advantage of the perpendicular embedded electrodes is the formation of a uniform and symmetric electric field resulting in less signal noise during measurement acquisition.[4]

Figure 4.3: The overlayed layers correspond to the lumen profile (red), membrane-basolateral adhesive profile (green), and the basolateral profile (blue). The profiles have an elongated cross-sectional region to increase sensing area and improve microscopy visualization. The membrane basolateral adhesive profile is slightly smaller than the cross-sectional region of the lumen and basolateral profiles as a control for chip-to-chip variation.

Figure 4.4: The μE-BBB is comprised of A) a lumen electrode, B) a lumen channel, C) a PC membrane, D) a membrane-basolateral adhesive layer, E) a basolateral layer, F) a basolateral electrode adhesive layer, and G) a basolateral electrode.[3]

Figure 4.5: The μE-BBB is seeded with astrocytes (yellow) on day 0, and with endothelial cells (pink) on day 2. By day 7, the μE-BBB is fully mature.[3]

Figure 4.6: The membrane was stained for cell growth for bEnd.3 cell growth after 5 days and for C8-D1A cell growth after 7 days. Both of these conditions demonstrate that by the end of the growth period, both cell lines have formed distinct monolayers covering the membrane. The bEnd. 3 cells are visibly confined within the narrow boundary of the

channel, while the C8-D1A cells extend outside the field of view of the microscope in the larger basolateral chamber.

Figure 4.7: Excised membranes were stained for cell line specific markers. The bEnd.3 cells were stained for TJ markers, ZO-1 and CLDN-5, after 5 days of growth and the C8-D1A cells were stained for astrocyte marker, GFAP, after 7 days of growth. DRAQ5 was used as a nuclear costain.[3]

Figure 4.8: Large particle transport assays through μE-BBB were conducted by passing 100 μg mL-1 of 10 kDa FITC-dextran solution through the lumen compartment of the system for 1 hour and quantifying the amount of FITC-dextran that had accumulated in the basolateral compartment ($n = 4$; Mann–Whitney two-tailed test; * signifies $p < 0.05$). Initially, there is little resistance to the diffusion of FITC-dextran into the basolateral compartment, but as the device matures the permeability of the system decreases. Data represented as mean ± standard error of mean (SEM).[3]

Figure 4.9: Utilizing the integrated electrodes of the system, TEER measurements were collected daily. During the first 2 days of culture, the astrocytes alone do not induce any change in resistance. However, the resistance begins to increase following incorporation of bEnd.3 cells after day 2 ($n = 8$). All data represented as mean ± SEM.[3]

Figure 5.1: ZO-1 (green) expression was monitored after incubation with NO donor SNAP, showing a decrease in ZO-1 expression in the treated condition. DRAQ5 (red) was used as a nuclear costain.[3]

Figure 5.2: To evaluate the effect of NO on the integrity of the barrier, 1 mm SNAP and FITC-dextran were circulated through the μE-BBB. The accumulated basolateral FITC-

dextran was quantified, indicating an increase in barrier permeability in the treated devices (n = 4).[3]

Figure 5.3: TEER evaluation of SNAP treated devices demonstrate a decrease in TEER values following the SNAP treatment, which further demonstrate damage to the μE-BBB (n = 4).[3]

Figure 5.4: To evaluate the behavior of erythrocytes in response to shear stress, a modified μE-BBB was utilized that only contains the shear inducing lumen channel. Image was adapted with permission from Biorender.com under a paid academic subscription.[3]

Figure 5.5: To quantify the production of NO by erythrocytes undergoing shear stress, isolated mouse erythrocytes, supplemented with NO probe DAF-FM, were circulated through the modified μE-BBB (n = 4). Under physiological shear stress conditions, there was no increase in the production of NO by young erythrocytes (n = 4). However, there was an increase in the production of NO from old mouse derived erythrocytes (n = 4). Mann–Whitney two-tailed test; ns, * signify $p > 0.05$ and $p < 0.05$, respectively. All data represented as mean ± SEM.[3]

Figure 5.6: To evaluate the effect of erythrocytes on the permeability of the BBB, isolated erythrocytes from young or old mice, supplemented with FITC-dextran, were circulated through the μE-BBB. The accumulated basolateral FITC-dextran demonstrates greater barrier permeability associated with old animal derived erythrocytes under physiological conditions (n = 4). Mann–Whitney two-tailed test; * signifies $p < 0.05$. All data represented as mean ± SEM.[3]

Figure 5.7: TEER analysis mirrors FITC-dextran permeability in the presence of erythrocytes from the different aged donors, demonstrating that the decrease in TEER was larger with old animal derived erythrocytes when compared to young animal derived erythrocytes under physiological conditions (n = 4). Mann–Whitney two-tailed test; ns, * signify $p > 0.05$ and $p < 0.05$, respectively. All data represented as mean ± SEM.[3]

Figure 5.8: To quantify extracellular Hb, human erythrocytes were circulated through the modified μE-BBB, and supernatant 520 nm absorbance was recorded to quantify free Hb. In relation to low shear conditions, young donor erythrocytes did not release more Hb than the low shear counterparts (n = 4), but old donor erythrocytes did (n = 4). Mann–Whitney two-tailed test; ns, * signify $p > 0.05$ and $p < 0.05$, respectively. All data represented as mean ± SEM.[3]

Figure 5.9: To further evaluate erythrocyte response to shear stress, young and old erythrocytes were circulated through the modified μE-BBB. After 1 hour, there was a greater prevalence of apoptotic cells in the old erythrocyte population.[3]

Figure 5.10: The accumulated basolateral FITC-dextran demonstrates greater barrier permeability associated with old donor erythrocytes in relation to young donor erythrocytes under physiological conditions (n = 4). Mann–Whitney two-tailed test; ns, * signify $p > 0.05$ and $p < 0.05$, respectively. All data represented as mean ± SEM.[3]

Figure 5.11: TEER analysis mirrors the trendlines of FITC-dextran permeability in the presence of human erythrocytes, with a decrease in μE-BBB electrical resistance associated with old-derived erythrocytes when compared to young-derived erythrocytes (n = 4). Mann–Whitney two-tailed test; * signifies $p < 0.05$. All data represented as mean ± SEM.[3]

Figure 5.12: To evaluate the impact of erythrocyte produced NO on the μE-BBB, eNOSi human erythrocytes were circulated through the μE-BBB, and FITC-dextran permeability shows no difference in the effect of young and old erythrocytes on the barrier (n = 4). Mann–Whitney two-tailed test; ns, * signify $p > 0.05$ and $p < 0.05$, respectively. All data represented as mean ± SEM.[3]

Figure 5.13: TEER analysis of eNOSi erythrocytes reaffirms the observation (n = 4). Mann–Whitney two-tailed test; ns, * signify $p > 0.05$ and $p < 0.05$, respectively. All data represented as mean ± SEM.[3]

Figure 5.14: The permeability of the μE-BBB to FITC-dextran was lower in conditions where the old erythrocytes had been treated with the eNOS inhibitor, compared to the untreated sample ($n = 4$). Mann–Whitney two-tailed test; ns, * signify $p > 0.05$ and $p < 0.05$, respectively. All data represented as mean ± SEM.[3]

Figure 5.15: There was a smaller decrease in TEER associated with this sample set (n = 4). Mann–Whitney two-tailed test; ns, * signify $p > 0.05$ and $p < 0.05$, respectively. All data represented as mean ± SEM.[3]

Chapter 1: Introduction to the Scope of the Thesis

The Problems of an Aging Population

Advances in modern medicine have greatly extended human life expectancy, with the most notable increases occurring within the past 150 years. In the latter half of the 19th century, life expectancy in the developed world was roughly between 40-50 years.[5] In the following century, life expectancy steadily increased and now stands at roughly 85 years, and it is not uncommon for one to reach their centennial years. However, life expectancy has plateaued in the past decade.[5] We as a society are faced with a new problem. There is now a greater and more pressing issue of new age-associated diseases and conditions that need to be addressed.

There are a myriad of age-associated diseased that include, but are not limited to, Alzheimer's disease,[6] Parkinson's disease,[7] various cancers[8,9] and autoimmune conditions[10] that have in recent years presented with a higher prevalence in the global population. Not only does this increase in disease prevalence place a significant personal strain on individuals, but there is also increased cost on the global healthcare infrastructure. Many of these age-associated conditions follow complex cellular pathways, and are not only difficult to treat, but are a taxing strain on global resources. Furthermore, there is a notable decrease in the quality of life as individuals age. Advanced age has a strong association with the deterioration of bodily systems such as the metabolic system,[11] muscular system,[12] neurosensory system.[11] Additionally, and most pertinent to this dissertation, advanced age has shown to have a very strong association with cognitive decline.[13–15]

The concept of healthy aging describes early interventions that may be taken to encourage a more productive transition into advanced age. Various groups have identified interventions that support heathy aging, such as early life physical activity[15] or the sufficient intake of -3 fatty acids.[16] A more thorough understanding of alternative interventions can lead to hugely beneficial societal implications.

Heterochronic Parabiosis and Blood Exchange

The genesis of this work stems from heterochronic parabiosis studies. Heterochronic parabiosis is the surgical joining of two organisms of two different disease states. For the duration of a parabiosis experiment, the two parabionts have a shared circulatory system, and it has been demonstrated in mice that this procedure can have restorative effects, such as alleviating radiation toxicity,[17] mitigating muscular dystrophy,[18] and also rejuvenating old animals.[19] It is observed that the healthy parabiont is able to alleviate some of the disease burden off of the afflicted partner.

Specifically, from the aging heterochronic parabiosis studies, a major limitation was identified early on. Due to the complexity of the procedure, it was difficult to identify what factors contributed to the rejuvenation of the old animal and the decline of the younger partner. While the two animals do share their circulatory system, the contributing factors that culminate to the observed aggregate effect of rejuvenation or decline are far more complex than blood factors alone. Through their joined circulatory system, the old parabiont has access to the young parabiont's organ systems. The old animal benefits from the young partner's liver for detoxification, renal system for secretion, lungs for oxygenation, and digestive track for nourishment.[20,21] The inverse is true as well for the younger parabiont, as that animal's organ systems are under a greater

functional burden. Additionally, through exposure to youthful pheromones the old parabiont would have improved neuronal health.[22,23] Furthermore, such studies have limited translatability.

Heterochronic blood exchanges between young and old mice have provided new insight into the biology at play in parabiosis. Similar to heterochronic parabiosis, Rebo et al. demonstrated that a single blood exchange between mice of different age groups results in the general rejuvenation of the old parabiont and general decline of the young parabiont across multiple germ layers (Figure 1.1).[1] This study removed the influence of shared organ access and demonstrated that returning the circulatory environment of an older animal to that of a younger state may result in rejuvenation.

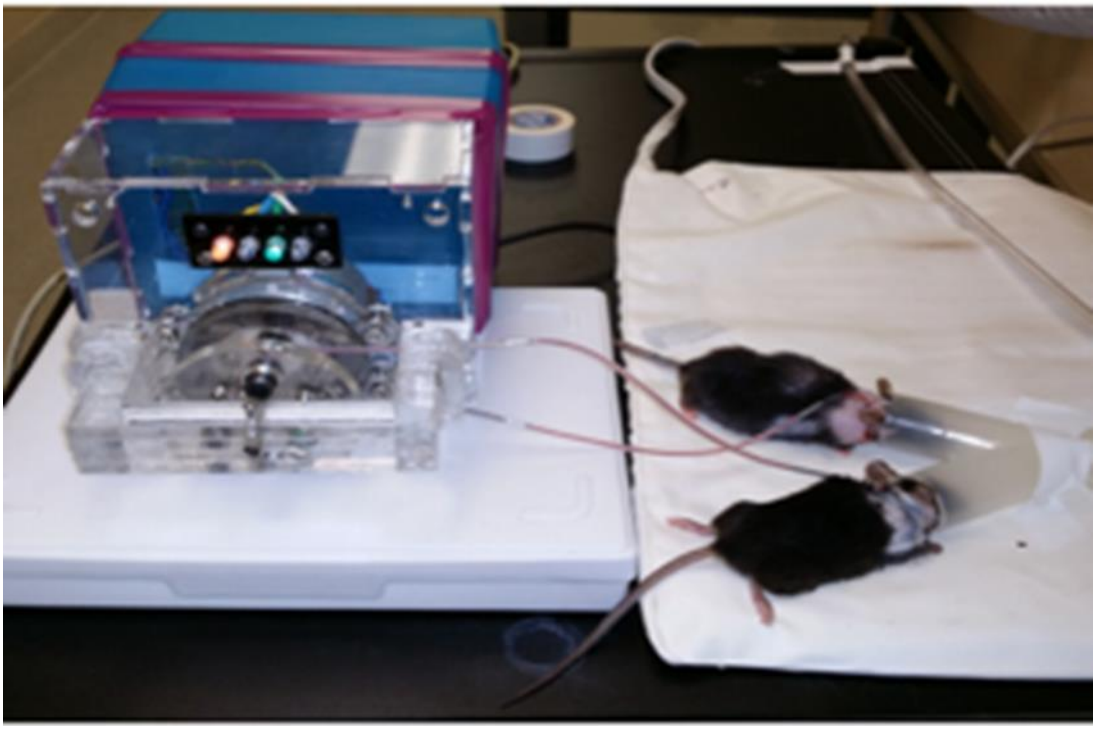

Figure 1.1: Blood exchange between young and old partners have demonstrated to have rejuvenative effects on blood exchange young and old partners.[1]

Returning to the previous discussed work on heterochronic blood exchange, the effect that heterochronic blood exchange had on the brain health of the animals was notable and most pertinent to the body of this dissertation. After exchange with an old partner, there was a drastic decline in neurogenesis in the young animal. However, there was no notable improvement in the levels of neurogenesis in the old animal (Figure 1.2).[1] This observation however raises a question. A healthy young mouse should have a properly fictional blood-brain barrier (BBB). If there were inhibitory factors in the blood of the old animal, the BBB of the young animal should have offered some protection for the young animal.[2,24,25] This suggests that there must have been factors in the blood of the old animal that caused the loss of BBB integrity.

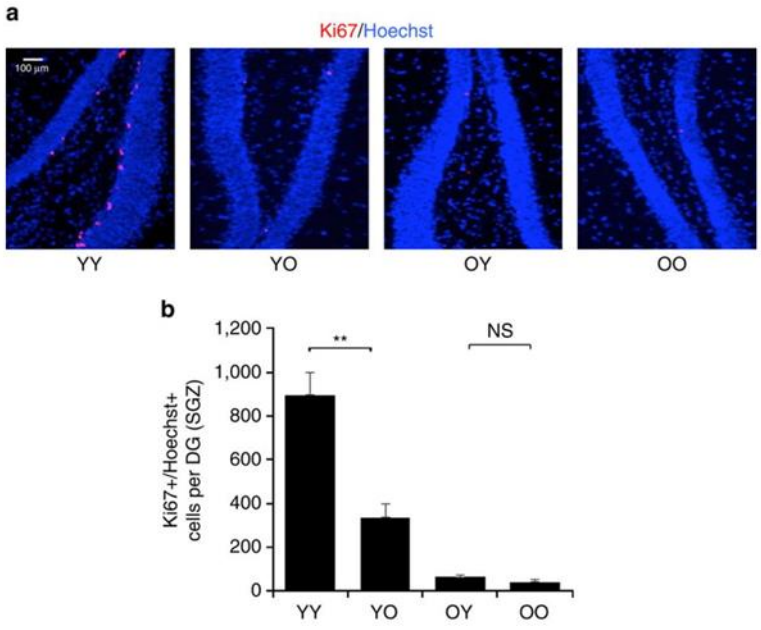

Figure 1.2: Following blood exchange between young and old mice, there was a significant decline in the young animal's hippocampal neurogenesis, but there was no observed improvement in the neurogenesis of the old animal.[1]

The BBB is characterized by tightly joined endothelial cells and supplemental basement membranes (Figure 1.3) .[2,24,25] It serves to isolate the central nervous system (CNS) from the circulating blood.[24] Specifically, the BBB presents high resistance to most blood-derived products to prevent their diffusion into the CNS. This is crucial as many circulating compounds are neurotoxic and/or neuro-inflammatory to brain health, such as fibrinogen[26] and TGF-β.[27] The tight junctions (TJs) of adjacent BBB endothelial cells play a pivotal role in maintaining its integrity.[28] It has also been shown that advanced age is associated with the decline in the integrity of the BBB[29,30] but the underlying pathologies leading to loss of BBB integrity with age are yet to be understood. In addition, several neurological diseases are associated with a compromised BBB, such as Alzheimer's disease,[25,30,31] Parkinson's disease,[25] multiple sclerosis,[32] and traumatic brain injury.[33].

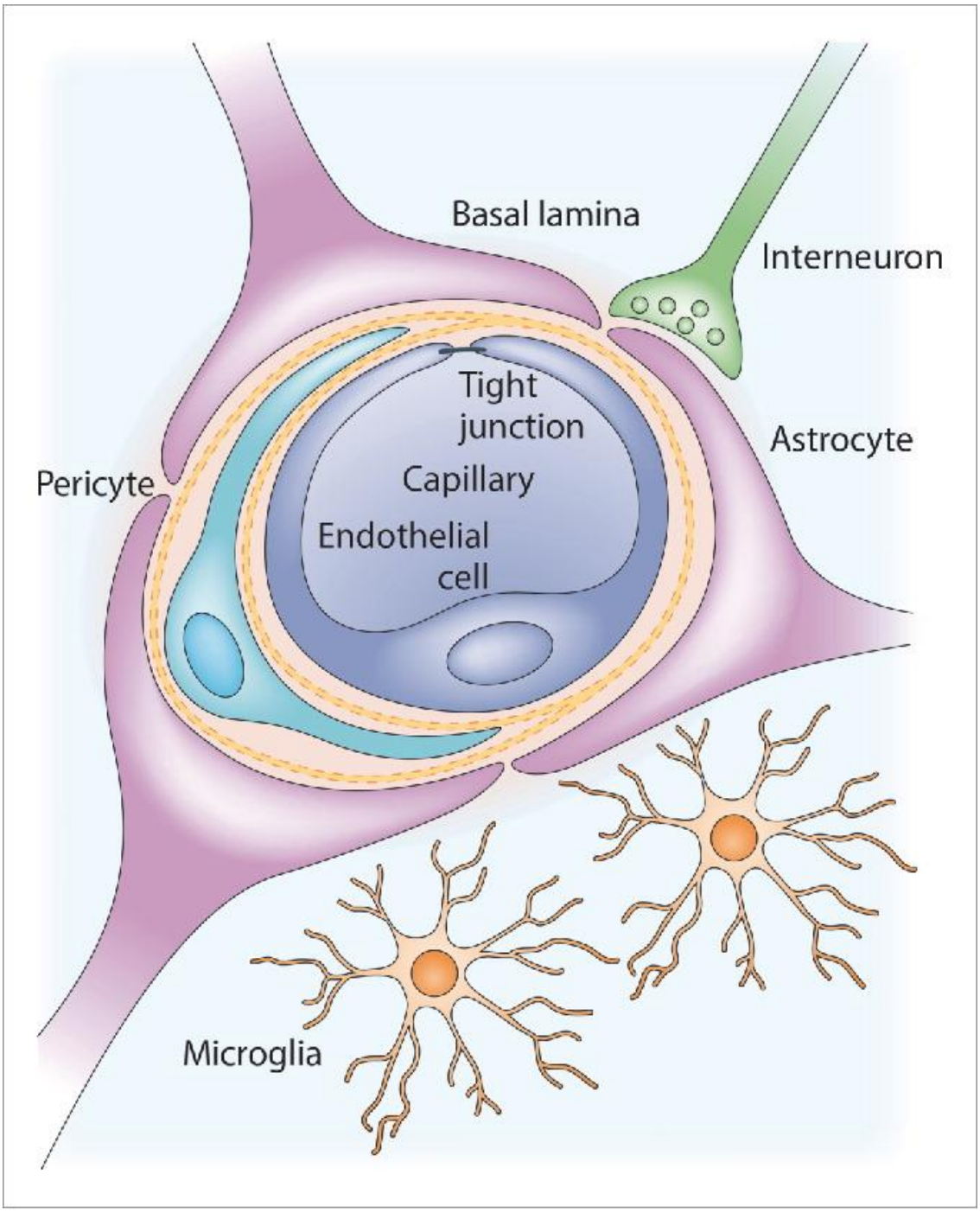

Figure 1.3: The BBB is composed of various cells, including endothelial astrocyte and pericyte cells. This structure separates the animal's circulating blood from the CNS.[2]

Erythrocytes

While the model of blood exchange improved upon parabiosis by reducing the number of contributing factors in the experiment, there are still limitations with the current model. Most notably, the composition of blood is extremely complex, with a variety of components that include leukocyte, plasma proteins, nucleic acids, exosomes and, with particular interest for this work, erythrocytes.[34–37] For the aim of this dissertation, I seek to provide evidence that identifies erythrocytes as a significant contributor to age associated neurological decline.

Erythrocytes, the most abundant cells in circulation, are vital gas transporters[38] and remain in the circulation for up to 120 days in humans and 60 days in mice. [39–42] As animals age, erythrocytes undergo significant morphological changes. For example, old erythrocytes (even when recently generated) are more rigid and less deformable than the erythrocytes produced by a young mammal. Studies corroborating this phenomenon encompass multiple animal models and experimental set-ups, including erythrocyte deformability and blood viscosity through centrifugal analysis and phase-contrast microscopy and membrane fluidity studies of erythrocyte ghosts.[43–47] Previously published computational and real-time microscopy research determined that when healthy young erythrocytes are subjected to a high shear stress environment, such as that of physiological capillaries, they deform from their native biconcave disk structure to a paraboloid.[48] Due to increased rigidity, erythrocytes of old mammals deform less readily, which is predicted to increase the shear stress on these cells (Figure 1.4).[46]

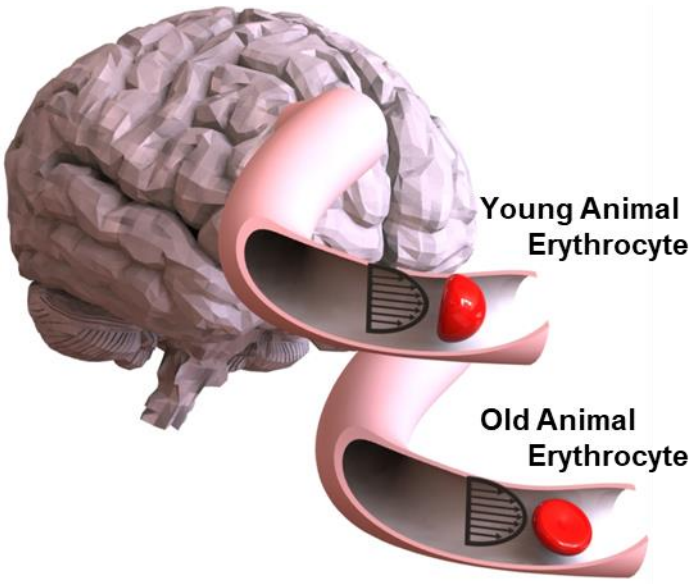

Figure 1.4: The erythrocyte membrane deforms to a paraboloid shape to better accommodate the shear stress in the capillary beds. Here, the black arrows depict the flow profile of shear stress forces. Erythrocytes from old animals (bottom) cannot deform as readily as young animal erythrocytes (top), due to their greater rigidity, and retain their discus shape.[3]

Erythrocytes are known to produce nitric oxide (NO) through their endothelial NO synthase (eNOS) membrane protein.[49] eNOS is one of the 3 NO synthase isoforms and was originally identified in the endothelial cells lining the blood vessels, but more recently has been identified in erythrocytes. Interestingly, the high levels of shear stress found in capillary beds increase the activity of eNOS, subsequently increasing the production of the reactive oxygen species and NO.[50] The primary purpose of this behavior is to induce vasodilation, and reduce local blood pressure, using shear stress as a surrogate marker.

The NO by erythrocytes has been implicated in increased permeability of the BBB.[51–54] Supporting these findings, antioxidants have shown to restore BBB function.[55,56] Furthermore, denser and more rigid erythrocytes produce more NO.[57] Additionally, erythrocytes in young mammals remain in circulation for a longer time, while in old animals erythrocytes have a higher turnover rate.[58–61] Tangentially, the lysis of erythrocytes releases hemoglobin (Hb) into circulation, and studies of cell-free Hb found strong associations with oxidative stress and BBB damage.[62,63]

Scope of Dissertation

To determine what role, if any, erythrocytes play in age-associated neurological decline, it will first be pertinent to develop the tools that will be necessary to conduct these experiments. The first shall be a programable device capable of blood fluidic handling. One purpose of a microfluidic blood handling system would be for the execution of future blood exchange procedures. There are many considerations that must be taken when working with mice, the first being the small blood volume of rodents. A rodent is estimated to have 58.5 mL/kg body weight of blood,[64] which results in less than 2 mL of total blood volume in a typical mouse. Any pump that would be used must be engineered to have a minuscule volume of dead space, as to minimize the volume extracted from the mouse. Additionally, the pump must be programable and bidirectional as to allow the user to set the volumes to be transferred and whether the blood is to be withdrawn or introduced. The blood handling system must also be reliable to a high confidence of less than 3% error. Due to the small blood volume of the mice, a compounding error in the fluidic handling of the blood can potentially invalidate a study.

The next aim of this dissertation is to develop a new microfluidic, organ-on-a-chip, technological platform for understanding the age-specific multiparametric effects of erythrocytes on the integrity of the BBB, connecting these effects with the changes in cell morphology, biochemistry, and viability. This is significant in investigating the role of systemic milieu in preventing or promoting the passage of molecules to the brain and, thus, the impact on neurological and age-associated disease.

The organ-on-a-chip will be a functional microfluidic BBB. The device will be designed in a way that it would mimic the shear inducing capillaries found in the brains of mice. BBB cells will be cultured within this device. After the cells have matured, BBB functionality is verified, and baseline measurements will be taken to monitor the metrics of the simulated BBB under healthy and damaged conditions. The second purpose of the microfluidic blood handling system would be for use in this novel organ-on-a-chip device.

Lastly, the microfluidic blood exchange system will be used with the organ-on-a-chip BBB to assess the effect of erythrocytes on the BBB. Erythrocytes will be drawn and isolated from young and old donors. These cells will be introduced into the validated system in order to identify what affect age has on the interaction between erythrocytes and the cellular structures of the BBB. A limitation of rodent studies is the difficulty to identify how different factors interact with each other. Furthermore, when investigating within a living organism, the researcher is hampered by the organism's innate function of maintaining homeostasis.[65–67] Through feedback-loops and systemic redundancies, organisms tend to be extremely robust at compensating for external stressors.

Chapter 2: The Development of the Microfluidic Blood Handling System

Parameters and Purpose of Microfluidic Blood Handling System

The microfluidic blood handling system is a peristaltic pump that is designed for two purposes: the transference of small volumes of blood between live mice and the fluidic control system for the BBB organ-on-a-chip. The engineered blood handling system is required to satisfy several criteria. The first is a dead space volume of no greater than 50µL. The blood handling system must also be programable and bidirectional. This allows the user to set the volumes to be transferred, and whether the blood is to be withdrawn or introduced. The blood handling system must also be reliable to a high confidence of less than 3% error. Due to the small blood volume of the mice, a compounding error in the fluidic handling of the blood can potentially invalidate a study.

To satisfy these requirements, the blood handling system will be constructed around the mechanics of a peristaltic pump.[68] A peristaltic pump falls under the category of positive displacement pumps. Generally, a peristaltic pump consists of a single flexible tube that is wrapped around the circumference of a pump head. The pump head has a series of rollers that make contact with a flexible tube. At the points of contact, the flexible tube is compressed, and the interior cavity closes. As the pump head rotates, the points of contact migrate down the length of the flexible tube, and the fluid trapped within the tube is either expelled or withdrawn in the direction of rotation.

This peristaltic pump design has several benefits over other pump models that make it better suited for the blood handling system.[68] The first is the ability to minimize the dead-space of the system to achieve a value of 50 µL or less. The dead-space of a

peristaltic pump is defined by the length and cross-sectional area of the tubing used in the system. This may be simply achieved with the use of microtubing. Furthermore, the cycle rate of the pump head and direction of rotation may be controlled with a simple micro-controller by altering the rate or sequence of motor steps.

Alternative positive pump designs include, but are not limited to, syringe or piston pumps,[69] diaphragm pumps,[70] or rotary pumps.[71] A major limitation of these models however are the large dead-spaces these systems require. Additionally, these models would require intricate components such as one-way-valves or gears that would be difficult to fabricate. Specifically for the piston and diaphragm pumps which require one way valves, the flow rate and direction of the pump would be difficult or impossible to adjust.[70] These are some of the reasons that these models were rejected for implementation in the microfluidic blood handling system.

The Design and Fabrication of the System's Mechanical Components

At the core of the blood handling system is a flexible silicone tube that is intermittently compressed by a series of rollers that are radially spaced around a rotating pump head. A motor controls the pump, which is used to withdraw blood from either a cannulated mouse or a blood suspension. As the rollers move along the silicone tube, blood is pulled into the pump and infused into either the mouse's exchange partner or the receiving reservoir. The transferred volume is a function of the silicone tubing internal diameter, motor step rate, and duration of exchange. The flow rate can be modified by adjusting the motor step rate. The flow rate of the system can be optimized to account for various factors which include, but are not limited to, fluid viscosity, blood exchange volume, hemolysis and coagulation.

To allow for application in multiple scenarios, two different pumps were designed—the first pump having a single pump head (Figure 2.1) and the second pump having 2 independent pump heads (Figure 2.2). Built from a similar underlying technology, the single pump has a smaller footprint and is easier to use in tighter areas. The dual pump is more robust as each head may move independently. This effectively allows it to perform all the functions of the single pump with the addition of performing multiple exchanges at once or more complex exchanges.

Figure 2.1: The single pump microfluidic blood handling system is a 3D printed device that features a single pump head.

Figure 2.2: The dual pump microfluidic blood handling system is a 3D printed device that features 2 independent pump heads.

The single-pump small animal blood exchange device consists of a 3D-printed hardware housing, dual rotating pump heads, pump head rollers, 22 gauge (22g) tubing connectors, and silicone tubing (Figure 2.3). The casing for the dual pump was 3D printed in three separate parts with an Ultimaker S5 using an acrylonitrile butadiene styrene (ABS) 2.85 mm filament, which was due to its high impact strength and impact resistance. Briefly, each part was designed with computer-aided design (CAD) software (SolidWorks) and printed through additive manufacturing path generated with the accompanying printer software (Cura). The layer height for the structures was set to 0.2 mm with a wall thickness of 2 mm, and the infill was set to 10%.

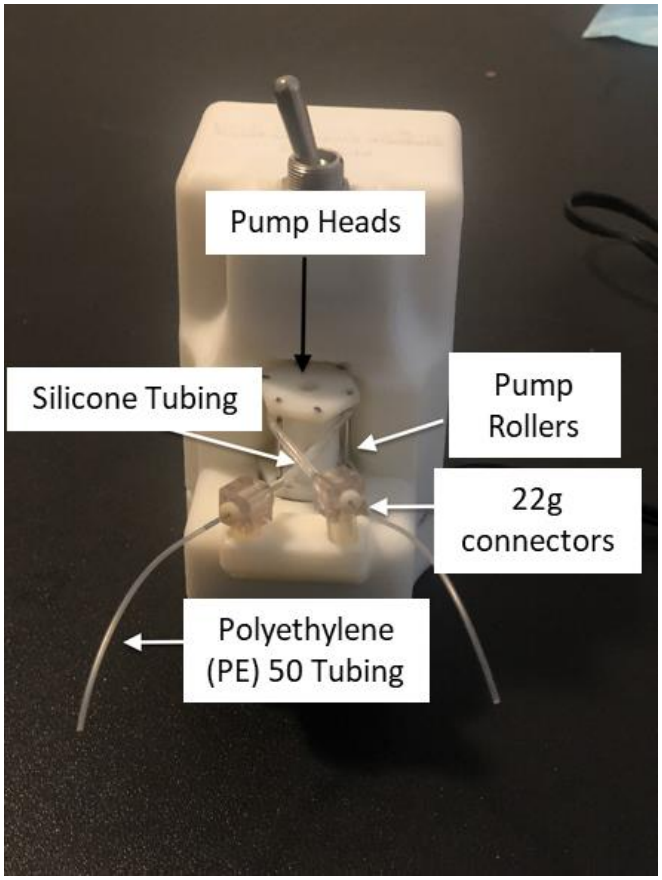

Figure 2.3: The 3D printed components of the single pump were designed to interact with a section of silicone tubing with a 22g inlet and outlet. The 22g connectors can connect to polyethylene-50 tubing, or 3 French polyurethane tubing.

Moreover, each part was designed to friction fit together as the final housing around the mechanical and electrical structures of the small animal exchange pumps. Similarly, the housing for the single pump is 3D printed in two separate parts with the same ABS filament and printer settings as described previously using the Ultimaker S5.

The dual pump was designed in a way that the three parts may pressure fit together. An additional two sets of pump heads were printed using the ABS filament

(Figure 2.4). In this case, the printed parts for the pump head are designed to fit together permanently using a two-part epoxy glue. The pump head(s) then pressure fit onto the stepper motor and are further secured with the two-part epoxy glue.

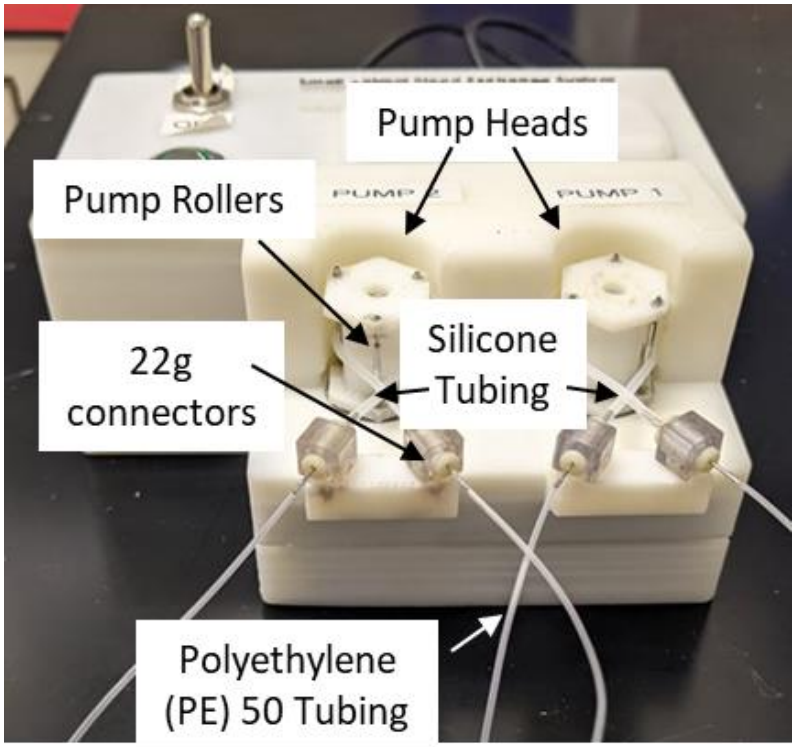

Figure 2.4: The 3D printed components of the dual pump were designed to interact with a section of silicone tubing with a 22g inlet and outlet per pump head. The 22g connectors can connect to polyethylene-50 tubing, or 3 French polyurethane tubing.

The pump head rollers were fabricated from 18-gauge (18g) and 22g hypodermic metal tubing. The 18g hypodermic tubing was used to create bushings that were fixed into the 3D printed pump head with the two-part epoxy glue. Placed within the bushings and fixed with the two-part epoxy, a section of 22g hypodermic tubing was used as a shaft. A section of 18g hypodermic tubing was set encompassing the 22g shaft and

allowed to freely rotate (Figure. 2.5). The free-rotating section of 18g hypodermic tubing was the component of roller that made contact and compressed the silicone tubing of the peristaltic pump, ultimately allowing for smooth fluid movement when pumping. Finally, a silicone oil lubricant was applied to the rollers to reduce friction.

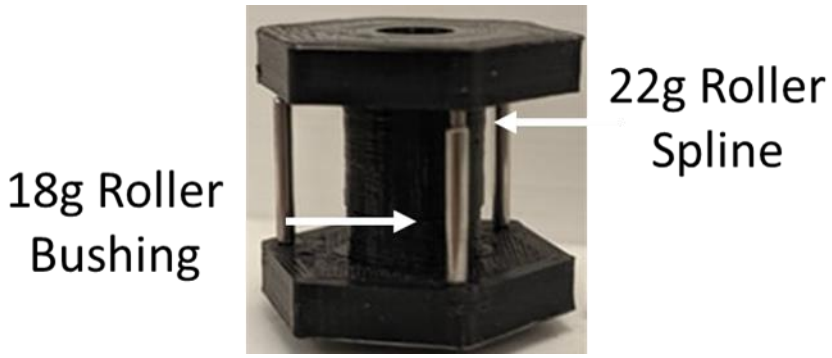

Figure 2.5: The pump rollers were fabricated from a section of 22g hypodermic tubing, nested within a 18g bushing. The free rotating bushing can make contact with the silicone tubing of the system without fraying or excessively damaging the silicone material.

To reduce mechanical friction and to prevent motor stalling, the pump head was lubricated using a silicone oil lubricant as well. This ensures smooth compression of the tube occurs to avoid ruptures. These characteristics improve the reproducibility and reliability of the system. Silicone tubing was used to wrap around the pump head (Instech; product number P720/TS-22020S22). The silicone tubing was subsequently crossed over to connect into the 3D printed socket in the pump body. Lastly, 22g connectors of the silicone tubing were used to connect the polyethylene (PE)-50 tubing (Instech; PE-50 tubing, 0.02in inner diameter x 0.083in outer diameter).

Electronics and Coding of Blood Handling System

Both pump systems are controlled by an Arduino Uno microcontroller electronic board that allows for both digital and analog input and output pins that can be integrated with different circuitry and an accompanying programmable computer code through an Arduino software.[72,73] Arduino is an open-source electronic software and hardware platform. The simple manipulation and customization of the Arduino platform makes it an attractive system to use for the development of the two pumps.

A stepper motor is well suited for this application as it allows for the conversion of electrical pulses into small discrete mechanical movements. Stepper motors are favorable for the case of small animal exchange devices in that stepper motors have extremely precise positioning and repeatability of movement within a 3-5% accuracy per step (with this error being non-cumulative with each successive step). Furthermore, stepper motors are ideal within exchange devices given there are no contact brushes in the motor, so the lifetime of the pump only relies on the lifetime of its bearings and is therefore extended compared to other pumps such as direct current (DC) motors.

Both systems were powered by a 12 watt (W) (12 volt (V)) alternating current (AC)-DC adaptor. The positive line for the adaptor was interrupted by a 2 ampere (A) blade fuse and a toggle switch, used to turn the system on or off. The blade fuse serves to protect the circuitry from any potential unexpected power surge.

The Arduino Uno for the single pump system was paired with a motor driver integrated circuit (L293D). The motor driver was connected to the single stepper motor and Arduino following the single pump wiring diagram. The AC-DC adaptor was used to

satisfy the power demands of the Arduino Uno microcontroller as well as the motor driver. The system was wired as described in Figure 2.6. Jumper wires were used to make the depicted connections for the system.

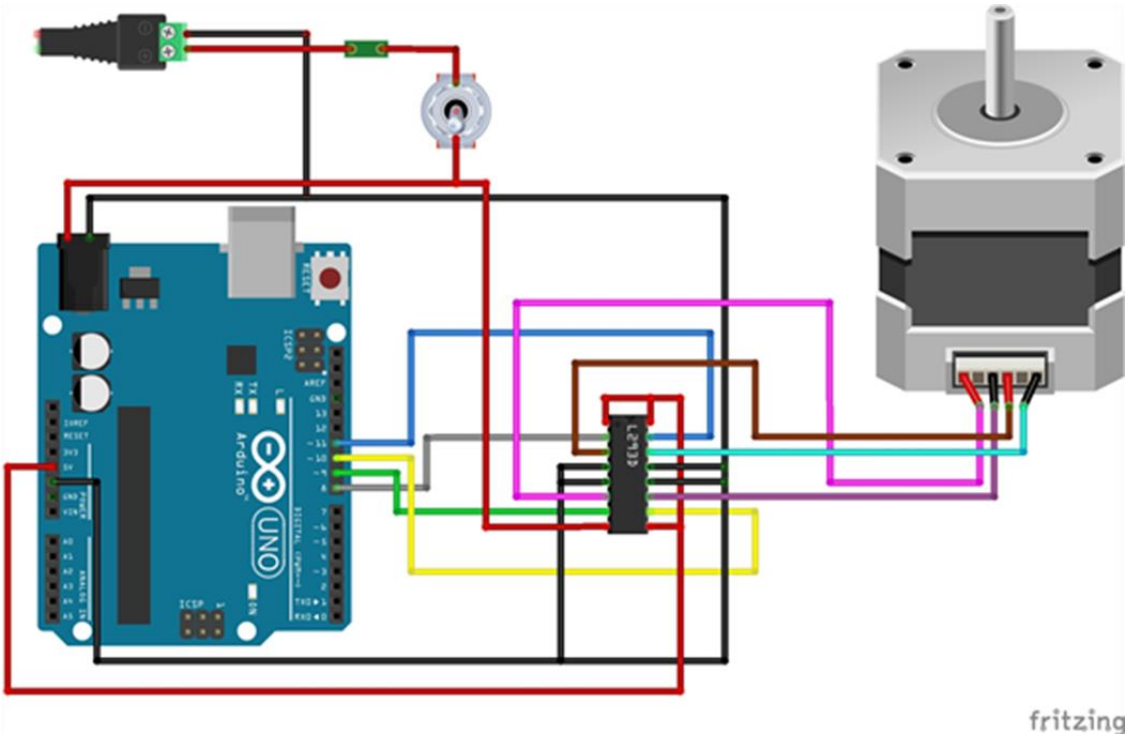

Figure 2.6: The wiring diagram of the single pump system allows for the single stepper motor to be controlled by the Arduino Uno through the motor driver.

Like the single pump system, the dual pump system was controlled by an Arduino Uno microcontroller and custom Arduino code to control the exchange volume, flow rate, and direction of fluidic handling. However, the dual pump was paired with an Adafruit motor shield. The motor shield functions in a comparable way to the motor driver for the single-pump device. The motor shield allows for the ability to control the direction and speed of the motor using the Arduino code to operate a single motor or both motors simultaneously. The motor shield was connected onto the Arduino using soldered single

row header pin connectors. To power the exchange device, the Arduino microcontroller utilized a 9V battery. The positive line for the battery was interrupted by a toggle switch, used to turn the system on or off. Similar to the single pump, the motor shield was powered by a 12W (12V) AC-DC adaptor, with the positive line for the adaptor interrupted by a 2A blade fuse. Finally, two stepper motors were used in this pump. Stepper motor one (SM1) was connected to the M1 and M2 terminal block of the Adafruit motor shield, and stepper motor two (SM2) was connected to the M3 and M4 terminal block of the Adafruit motor shield. The wiring diagram for the dual pump is described in Figure 2.7.

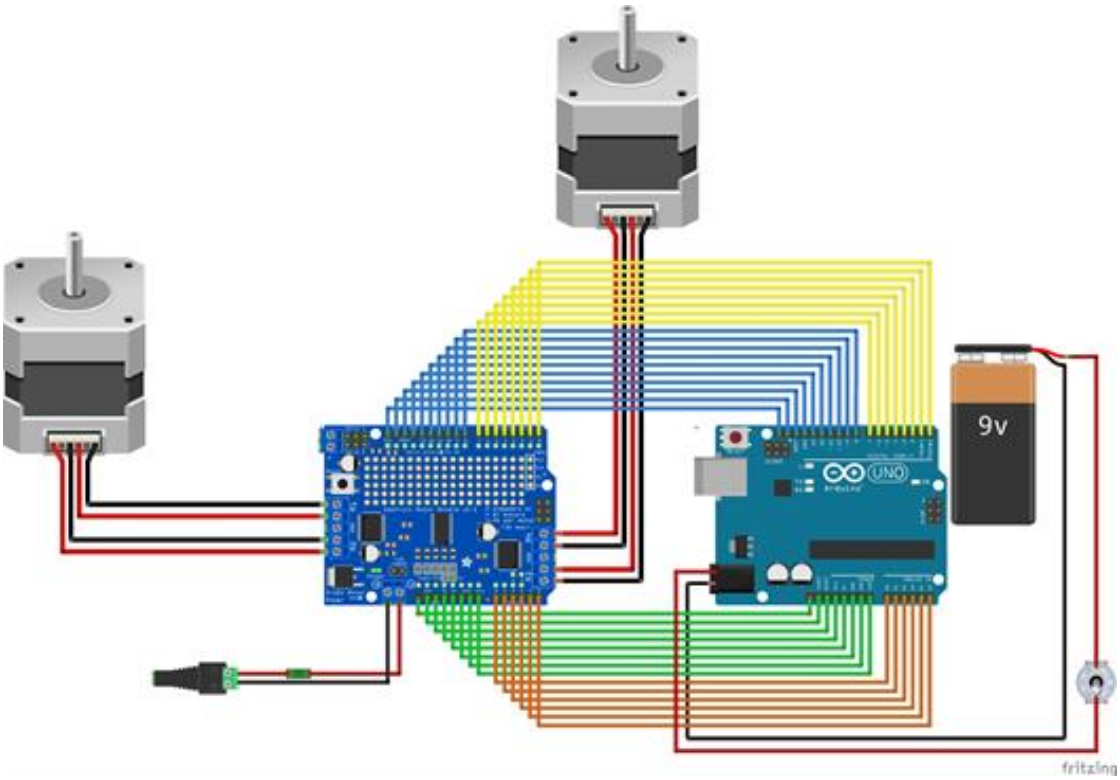

Figure 2.7: The wiring diagram of the dual pump system allows for the 2 stepper motors to be controlled by the Arduino Uno through the Adafruit motor shield.

Custom Arduino codes were written for each system using the Arduino IDE software. The first code compiled to control the single pump (Figure 2.8). To improve the usability of the code, the code contains a series of variable that may be adjusted to achieve the desired parameters. The first variable is *"half_cycle."* This variable correlates to the volume that the pump is programed to dispense and must be calibrated empirically due to variations in silicone tube elasticity. Increasing this value results in an increase in the volume dispensed, and a decrease in this variable reduces the volume dispensed. This value should also be divisible by 66.6 to account for the number of steps per full rotation of the stepper motor. The second variable is the number of full exchanges that are desired and may be modified by adjusting the variable *"exchange_number."* The variable *"slack"* is a constant and accounted for the lack in tension in the silicone tubing prior to the pump changing direction when exchanging blood. The *"delay_"* variable controls the speed. Increasing the delay, in steps of 5, slows the speed of the motor, and reducing the delay number increases the motor speed. The code is designed to run automatically when the system is turned on and will cease pumping as soon as the desired number of exchanges has been satisfied.

```
#include <Stepper.h>
const int stepsPerRevolution = 200;
// change this to fit the number of steps per revolution
// for your motor
Stepper myStepper(stepsPerRevolution, 9, 10, 11, 12);
// initialize the stepper library on pins 9 through 12:
void setup() {
 Serial.begin(9600);
 myStepper.setSpeed(20);
const int half_cycle = 9933;
 //adjust number of steps here (divisible by 66.6)
 //increase number to increase the volume exchanged
 //decrease number to decrease the volume exchanged
const int exchange_number = 10;
 // input number of exchanges
const int slack = 200;
 //error for slack
const int delay_ = 30;
 // delay between steps, higher delay -> slower speed, divisible by 5
 // if delay is adjusted, the number of steps must be changed as well
myStepper.step (half_cycle - slack);
delay(delay_);
for (int x = 0; x < (exchange_number - 1); x++) {
 myStepper.step(-(half_cycle));
 delay(delay_);
 myStepper.step(half_cycle);
 delay(delay_);
}
 myStepper.step(-(half_cycle));
 delay(delay_);
}
void loop() {}
```

Figure 2.8: The code for the single pump is directed by 4 variables, that the user may adjust to calibrate the system or modify the parameters for the desired experiment.

Since the dual pump is controlled through the Adafruit Motor Shield, as opposed to the motor driver, a different code is required to operate the system. The code however was written in a similar manor to the single pump, where the parameters and calibration are controlled through the same 4 variables. *"Half_cycle," "exchange_number," "slack"*

and *"delay_"* are present in this code and carry the same definitions. There are 2 variations of the code for the dual pump, however. The first being a variation that only controls a single pump, while the other remains idle. That code is represented in Figure 2.9. An additional variable for this program is the specification of which pump needs to be used. To do this, the myMotor and getStepper values need to be adjusted to select either pump head 1 or 2.

```
#include <Adafruit_MotorShield.h>
#include "utility/Adafruit_MS_PWMServoDriver.h"
#include <Stepper.h>
Adafruit_MotorShield AFMS = Adafruit_MotorShield();
Adafruit_StepperMotor *myMotor1 = AFMS.getStepper(200, 1);
//Specify myMotor1 or myMotor2 depending on which pump is to be used
//myMotor2 is activated by "Adafruit_StepperMotor *myMotor2 = AFMS.getStepper(200, 2);"
void setup() {
 Serial.begin(9600);
const int half_cycle = 9933;
 //adjust number of steps here (divisible by 66.6)
 //increase number to increase the volume exchanged
 //decrease number to decrease the volume exchanged
const int exchange_number = 10;
 // input number of exchanges
const int slack = 200;
 //error for slack
const int delay_ = 30;
 // delay between steps, higher delay -> slower speed, divisible by 5
 // if delay is adjusted, the number of steps must be changed as well
 myMotor1->setSpeed(40);
  //Specify myMotor1 or myMotor2 depending on which pump is to be used
 AFMS.begin();
 myMotor1->step(half_cycle - slack, FORWARD, SINGLE);
  //Specify myMotor1 or myMotor2 depending on which pump is to be used
 delay(delay_);
for (int x = 0; x < (exchange_number - 1); x++) {
 myMotor1->step(half_cycle, BACKWARD, SINGLE);
  //Specify myMotor1 or myMotor 2 depending on which pump is to be used
 delay(delay_);
 myMotor1->step(half_cycle, FORWARD, SINGLE);
  //Specify myMotor1 or myMotor2 depending on which pump is to be used
 delay(delay_);
}
 myMotor1->step(half_cycle, BACKWARD, SINGLE);
  //Specify myMotor1 or myMotor2 depending on which pump is to be used
 delay(delay_);
}
void loop() {}
```

Figure 2.9: To only use a single pump from the dual pump, 4 variables are used to control the system that the user may adjust to calibrate the system or modify the parameters for the desired experiment. The specific pump may also be selected.

The second variation of the dual pump code is depicted in Figure 2.10. In this program, the code is written similarly to that of the single action dual pump, with the exception of the user no longer needing to specify which pump head needs to be selected as active.

```
#include <Adafruit_MotorShield.h>
#include "utility/Adafruit_MS_PWMServoDriver.h"
#include <Stepper.h>
Adafruit_MotorShield AFMS = Adafruit_MotorShield();
Adafruit_StepperMotor *myMotor1 = AFMS.getStepper(200, 1);
Adafruit_StepperMotor *myMotor2 = AFMS.getStepper(200, 2);
void setup() {
  Serial.begin(9600);
const int half_cycle = 9933;
  //adjust number of steps here (divisible by 66.6)
  //increase number to increase the volume exchanged
  //decrease number to decrease the volume exchanged
const int exchange_number = 10;
  // input number of exchanges
const int slack = 200;
  //error for slack
const int delay_ = 30;
  // delay between steps, higher delay -> slower speed, divisible by 5
  // if delay is adjusted, the number of steps must be changed as well
  myMotor1->setSpeed(80);
  myMotor2->setSpeed(80);
  AFMS.begin();
  for (int a = 0; a < (half_cycle - slack - 1); a++) {
  myMotor1->step(1, FORWARD, DOUBLE);
  delay(5);
  myMotor2->step(1, FORWARD, DOUBLE);
  delay(5 + delay_);
}
for (int x = 0; x < (exchange_number - 1); x++) {
for (int b = 0; b < (half_cycle); b++) {
  myMotor1->step(1, BACKWARD, DOUBLE);
  delay(5);
  myMotor2->step(1, BACKWARD, DOUBLE);
  delay(5 + delay_);
}
for (int c = 0; c < (half_cycle); c++) {
  myMotor1->step(1, FORWARD, DOUBLE);
  delay(5);
  myMotor2->step(1, FORWARD, DOUBLE);
  delay(5 + delay_);
}
}
for (int d = 0; d < (half_cycle); d++) {
  myMotor1->step(1, BACKWARD, DOUBLE);
  delay(5);
  myMotor2->step(1, BACKWARD, DOUBLE);
  delay(5 + delay_);
}
}
void loop() {}
```

Figure 2.10: To only use both pumps from the dual pump, 4 variables are used to control the system that the user may adjust to calibrate the system or modify the parameters for the desired experiment.

Validation and System Calibration

Calibration of these systems was conducted using two different exchange models under various exchange conditions. The first being the "back-and-forth exchange" model where blood is being exchanged between two mice in a simple back-and-forth fashion. A limitation of this experimental setup is that with each exchange, the native blood of each mouse is diluted with that of the partner. Therefore, the actual volume of foreign blood both mice are receiving with each exchange is diminished, eventually reaching an asymptote. The second model is the "extraction-replacement exchange" model. With this experimental set up, a single mouse received blood from a vial of donor blood. After each infusion, the volume being withdrawn from the mouse is discarded. This prevents the donor stock of blood from being diluted with the native blood of the mouse. This model however cannot be implemented in the exchange between 2 live partners.

The calibration exchanges were conducted using sample aliquots of water with and without red food coloring to simulate two different mice, either of similar (34 g and 34 g) or different weights (34 g and 28 g) (Figure 2.11). Furthermore, the exchange was also simulated for a single 34g mouse using the extraction-replacement model (Figure 2.12). The blood volume for the mice can be estimated using the calculation at 58.5 mL/kg of body weight.[64] Following a predetermined number of exchanges, samples from each aliquot were colorimetrically quantified using an absorbance plate reader (520 nm).

Blinded studies were compared to mathematical models provided generated by the Conboy Lab (UC Berkeley).

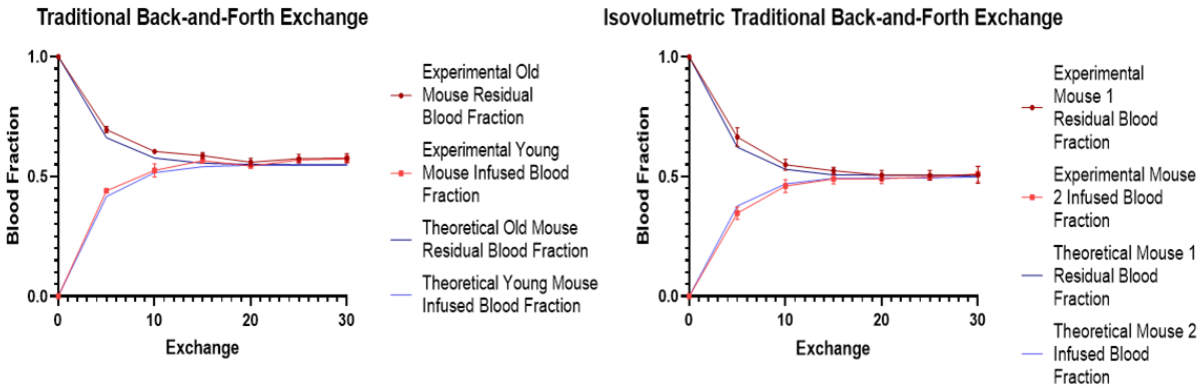

Figure 2.11: Back-and-forth simulation exchanges were conducted between mice of different or similar sizes, and the percent exchanged was compared to a mathematical model.

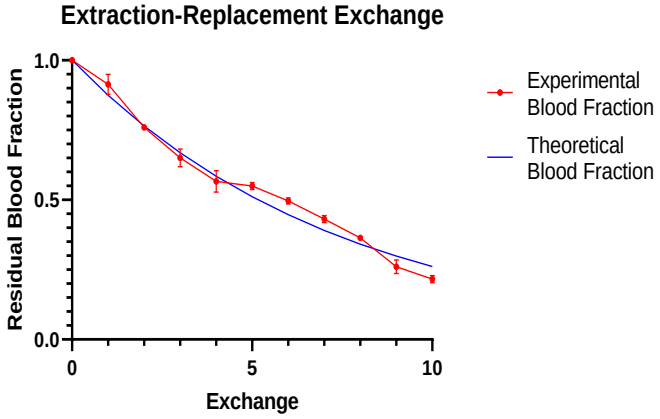

Figure 2.12: Extraction-replacement simulation exchanges were conducted between a simulated mouse and a stock of simulated blood, and the percent exchanged was compared to a mathematical model.

To implement either system for blood exchange (Figure 2.13), there are several crucial steps. The first being the calibration of the pump. Variations in the elasticity of the flexible silicone tubing alters the flow rate of the system, even when the programed step rate is unchanged. Variations in the elasticity may be primarily attributed to the use and wearing of the tubing from repeated exchanges. To lessen the impact of this phenomenon, the lines should be stored in a non-tensioned position. To calibrate the pump, the system should be connected to 5 cm long sections of PE-50 tubing on each end. The lines should be filled with a neutral solution, and the inlet tube should be placed in a revisor of the same solution. The outlet may be placed in an empty microcentrifuge tube. The pump should then be turned on and allowed to run until the flow changes polarity. The volume in the outlet tube should be measured. If the volume needs to be adjusted, the Arduino code should be modified as described previously. “Const int half_cycle = xxxx” describes the number of motor steps that the system outputs for a single direction exchange. Increasing this number increases the exchange volume and decreasing this value reduces the volume exchanged. It should be noted that the dead space for the system is 50 µL. For any amount of volume exchanged, the effective exchange would be that volume minus 50 µL.

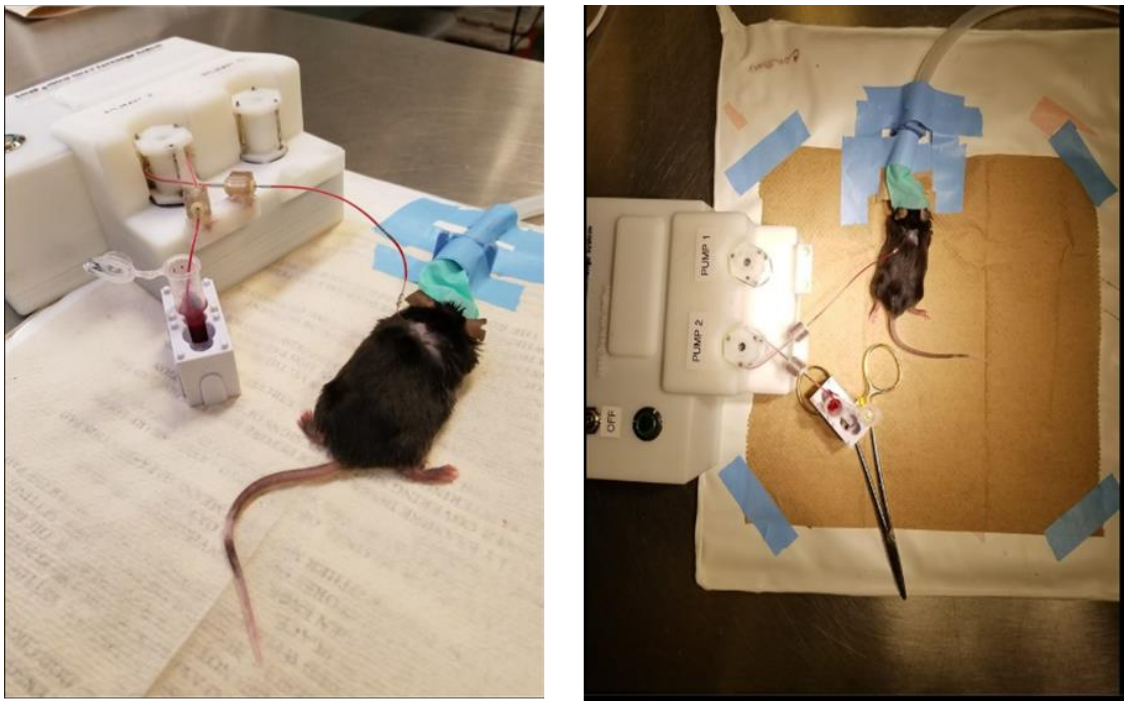

Figure 2.13: To execute an *in vivo* blood exchange, a mouse needs to be connected to the blood handling system via a surgically placed jugular vein catheter.

The second critical step for the implementation of this system is to prevent the incidence of coagulation and blockages within the system. Empirically, it has been observed that metal encourages blood aggregation and heparin coating can limit this phenomenon. However, there are still situations when aggregation can occur. Heparin coating is accomplished by filling the line with 10 units/mL of heparin in normal saline overnight with the open ends of the lines joined with a 22g coupler.

Chapter 3: The Development of the First-Generation Blood-Brain Barrier Organ on a Chip

Device Design and Fabrication

The first generation of the BBB organ-on-a-chip was created to observe the interaction of erythrocytes with brain endothelial cells in a physiologically relevant, high shear environment, and to be able to observe the effect of these erythrocytes on the endothelial cells. To do this, the device was designed to be composed of 3 layers: a glass substrate layer with interdigitated electrodes, a middle thin culture well layer, and the shear inducing capillary layer on top (Figure 3.1).

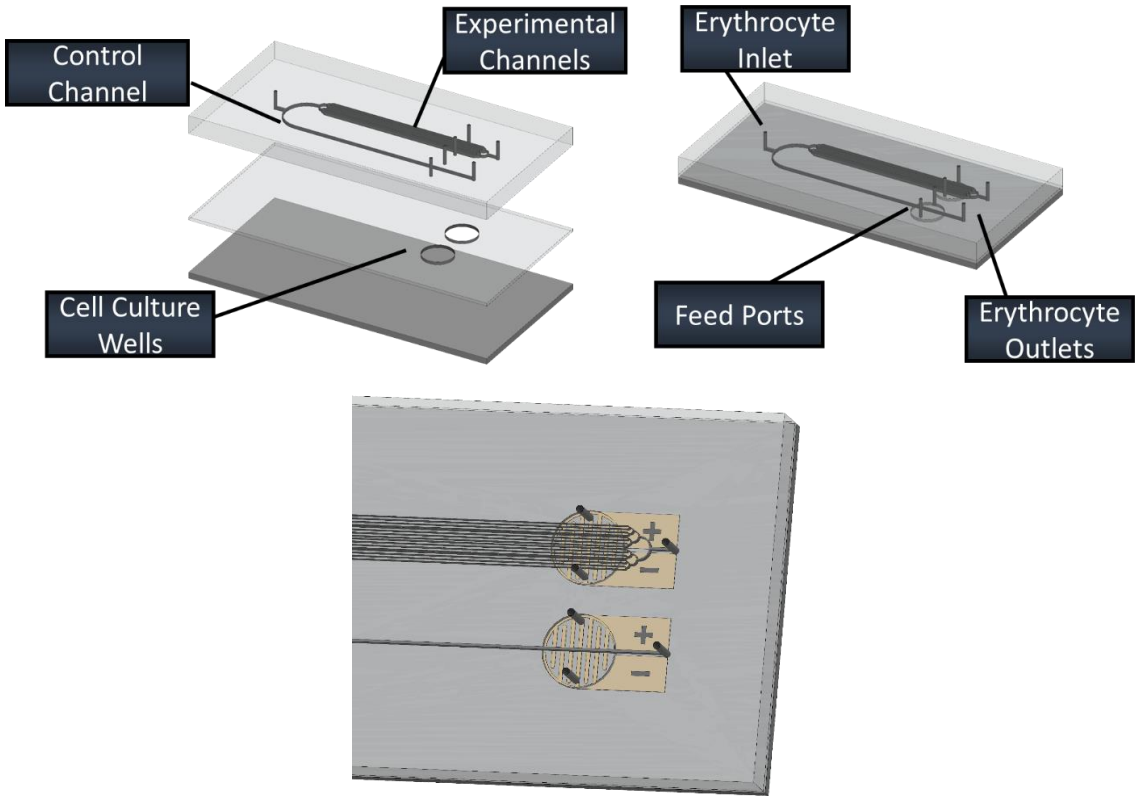

Figure 3.1: The BBB organ-on-a-chip device is composed of three layers. The endothelial cells may be able to grow within the culture wells of the device and

interact with erythrocytes that are perfused through the channels in the upper layer. The cells grown within the device will grow over interdigitated electrodes.

Interdigitated electrodes are two individual electrodes that form a comb-like structure. The structures are mirrored from each other and offset by a half electrode pitch (Figure 3.2). The interdigitated electrodes were built from the technology of trans epithelial electrical resistance (TEER). TEER operates based off of the principle, that as the confluency of the cells in culture increase, specifically that of endothelial cells, there would be an increase in electrical resistance between the electrodes that flank the cells. This is because of the tight junctions that the endothelial cells form, which limit the free passage of ions between the electrodes. The gold interdigitated electrodes were produced in collaboration by Dr. Jacobo Paredes. In brief, the electrodes were fabricated with standard lithography methods. An SU-8 layer was deposited onto gold slides that featured structures negative to that of the final design. 10 nm chromium was sputtered onto the glass, followed by 50 nm of gold. The SU-8 layer was removed, leaving behind the final interdigitated electrodes.

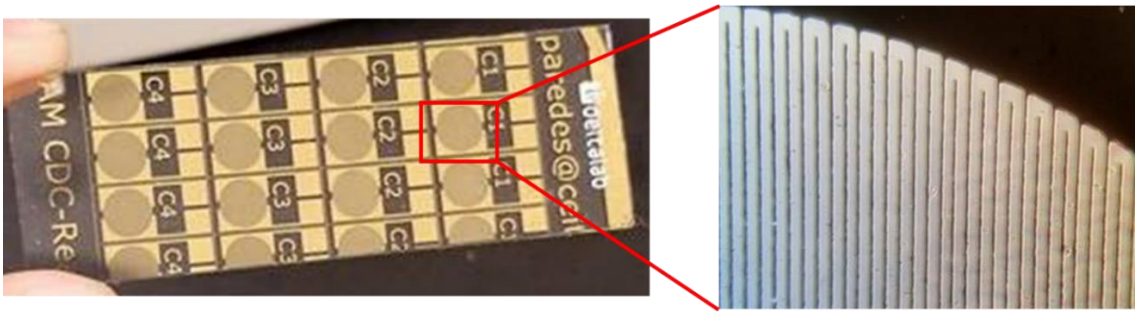

Figure 3.2: The interdigitated electrodes are featured on a standard glass slide. Each electrode set is composed of two independent electrodes that form a comb-

like structure. The off-set electrodes can be used to monitor the electrical resistance of a cell culture monolayer.

The middle layer is a thin polydimethylsiloxane (PDMS) layer that was designed to overlap with the interdigitated electrodes. These regions are crucial to allow adequate room for the cells to grow a uniform monolayer over the electrodes, without obstructing the microchannels of the top layer. This layer was designed to be 50 μm in height.

The top channel of the device was built to feature the shear inducing microcapillaries. From a single inlet, two channels branched out to form the control and experimental conditions with each condition connected to a unique outlet. The experimental channels were a set of 16 channels 10.2 μm in diameter, and the single control channel had a diameter of 163.2 μm. The height of these channels was designed to be 15 μm. The experimental channels were modeled after the physiological diameter of mouse brain microcapillaries. This was done to ensure sample uniformity between control and experimental conditions. To ensure similar flow profiles between the channel sets the cross-sectional area between the channels and the culture wells was kept equal. Following Poiseuille's Equation ($\tau=(4\eta\cdot Q)/(h^2\cdot w)$), the shear stress within a channel is primarily an exponential function that is primarily driven by the width or the height, whichever value is smaller.[74] Due to this formula, the theoretical shear value for each of the experimental channels could be estimated as roughly 23.5 times greater than that of the control channel.

To optimize culture techniques and experimental protocols, different variations of this device were fabricated. The first version was the culture-only device (Figure 3.3). The culture-only device is composed of 2 layers: a glass substrate, and a PDMS layer that

contained the features of the culture wells. The features were fabricated using standard soft lithography techniques and SU-8 2025 to create 50 µm tall features. This device was for the purpose of optimizing cell culture techniques within a microfluidic device.

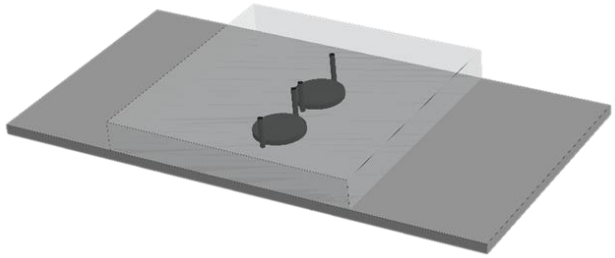

Figure 3.3: The culture-only device consists of a single PDMS layer bound to glass. The PDMS contains features that serve as culture well and the purpose of this device is to optimize cell culture methodologies.

The second device was the culture-channel device (Figure 3.4). This device featured the same PDMS culture well layer as the previous version, but it was instead bound to a layer of PDMS that featured the control and experimental channels. The channel layer was fabricated using standard soft lithography techniques and SU-8 2015 to create 15 µm tall features. This device was for optimizing the experiment protocol, by allowing cultured cells to interact with erythrocytes flowing through the channels.

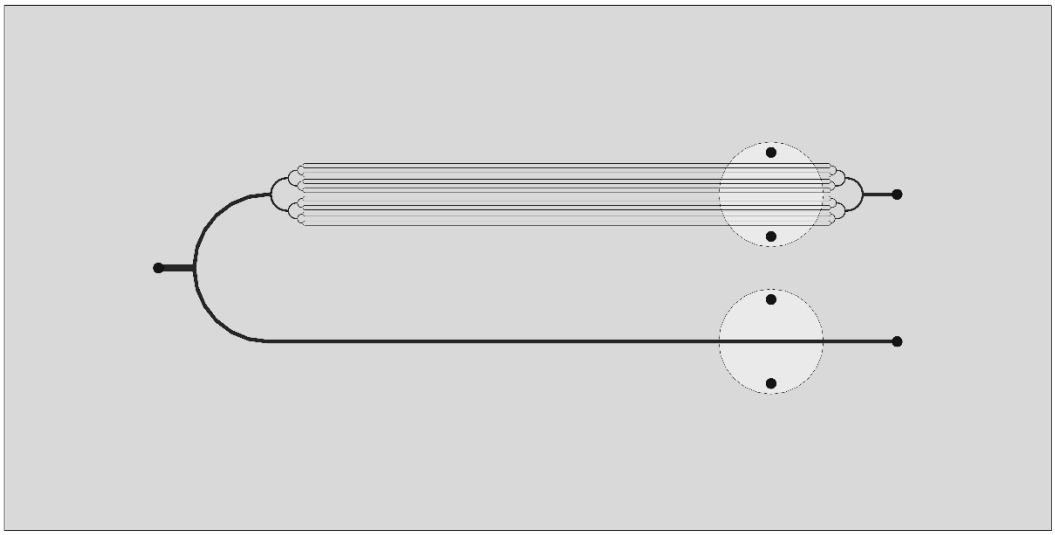

Figure 3.4: The culture-channel device is a combination of the PDMS cell culture well structures of the previous device with the PDMS thin channel structures. The device does not contain the TEER interdigitated electrodes and the cells in this device are grown on PDMS. The purpose of this device is to optimize experimental protocols.

The third and ultimate iteration of the device was the complete structure (Figure 3.1). For this, the channels were fabricated in the method previously described. However, the central culture well was fabricated using spin coated PDMS on a glass slide with holes punched to define the culture wells. By spin coating the PDMS on a glass substrate at 1500 rpm, a thickness of 50 µm could be achieved.[75] The thin PDMS layer was bound to the channel layer, and then delaminated from the glass surface. The newly exposed surface of PDMS was then bound to the glass interdigitated TEER electrode layer.

For all devices, the layers were covalently bonded together using the piezo torch method as described by Ghaemi et al.[76] Inlets and outlets were created by first punching a hole through the PDMS with a 0.75 mm biopsy punch (WPI, 504529). PE-50 tubing was

then inserted into the hole and a 2-part epoxy was used as a sealant. The tubing used was connected to syringes fitted with a 22g coupler.

Culture Optimization

Mouse brain endothelial bEnd.3 cells were grown in Dulbecco's Modified Eagle Medium (DMEM) containing 10% fetal bovine serum and 1% Antibiotic-Antimycotic solution vacuum filtered through a 0.22 μm polyvinylidene fluoride filter (complete growth media). The cells were grown in T-75 culture flasks and grown to 70–90% confluency. The cells were passaged with 0.25%Trypsin/0.2%EDTA and grown in a 37 °C incubator under 5% CO_2.

For this device, the cells used were the bEnd.3 mouse brain endothelial cell line, and culture techniques were optimized using the culture-only device. The first step was to sterilize the device. This was done by flushing the device with 70% ethanol (EtOH). This was followed by a wash of 1x phosphate buffered saline (PBS). The device was then incubated with 50 μg/mL fibronectin and allowed to incubate within an incubator for 1 hour at 37 °C. This was followed by a flush with complete growth media. The device was allowed to incubate for 2 hours with the media at 37 °C, as it was observed that this led to an improvement in cell adhesion. After this incubation step, the bEnd.3 cells were introduced to the device at the concentration of 6e4 cells/cm^2, achieved by suspending the endothelial cells to a concentration of 1.2e7 cells/mL. The cells were placed into the incubator under static conditions to allow the cells to adhere to the functionalized surface of the device. After 3 hours, the device was perfused with complete growth media at a rate of 0.5 μL/min. The cells were allowed to grow for 5 days to reach full maturation (Figure 3.5).

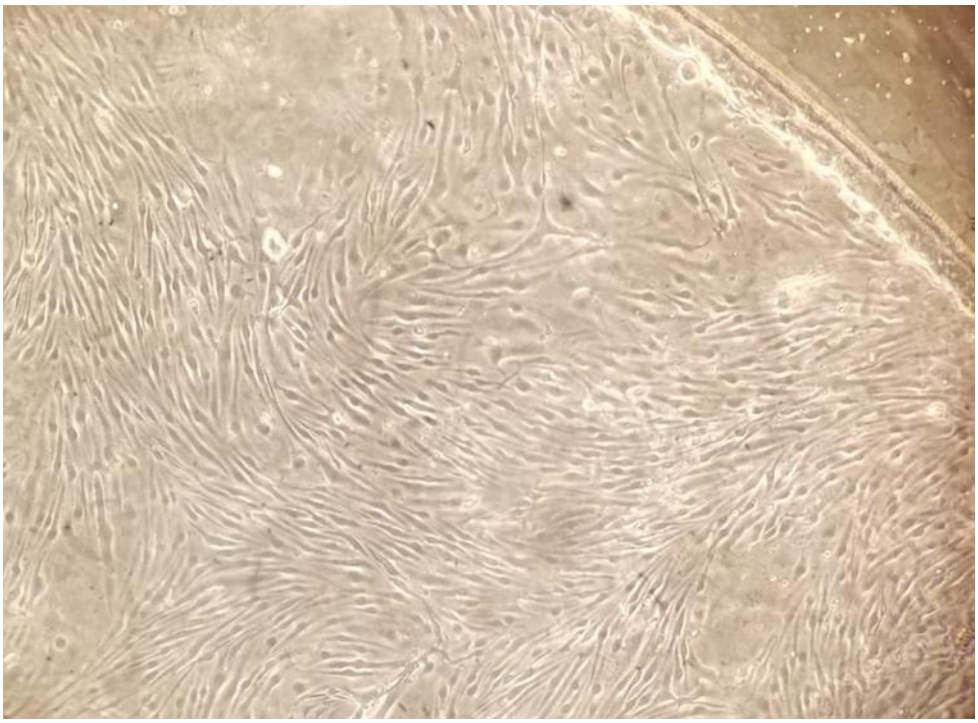

Figure 3.5: After 5 days of culture, the endothelial cells have become fully confluent and adopted a striated conformation. The cells are confined to the growth region and do not grow past the PDMS wall on the upper right corner of the figure.

Maturity was initially confirmed by immunocytochemistry (ICC) staining. This was accomplished by first arresting cell growth and fixing the bEnd.3 cells. Ice cold 4% paraformaldehyde (PFA) in PBS was perfused through the device and the device was allowed to sit over ice for 15 minutes. It was observed that the PFA had the effect of degrading the bond between the PDMS and the glass slide, allowing for the PDMS layer to be peeled off. This was then followed by a wash with PBS and blocking with 5% bovine serum albumin (BSA) for 1 hour at room temperature. The bEnd.3 cells were incubated with Alexa 488 conjugated zonula occludens-1 (ZO-1) (Santa Cruz, sc-33725 AF488) antibodies at a 1:100 dilution in 0.75% BSA in PBS overnight at 4 °C. Cells

were washed with PBS and costained with DRAQ5 (Invitorgen, 62251) at a 1:200 dilution in PBS for 30 minutes at room temperature. The membrane was mounted in fluoromount, and images were taken with the Opera Phenix Microscope (Figure 3.6). After 5 days of growth, the bEnd.3 cells are highly confluent and are strongly expressing the ZO-1 TJ marker at the cell-to-cell junction, indicating a positive stain.

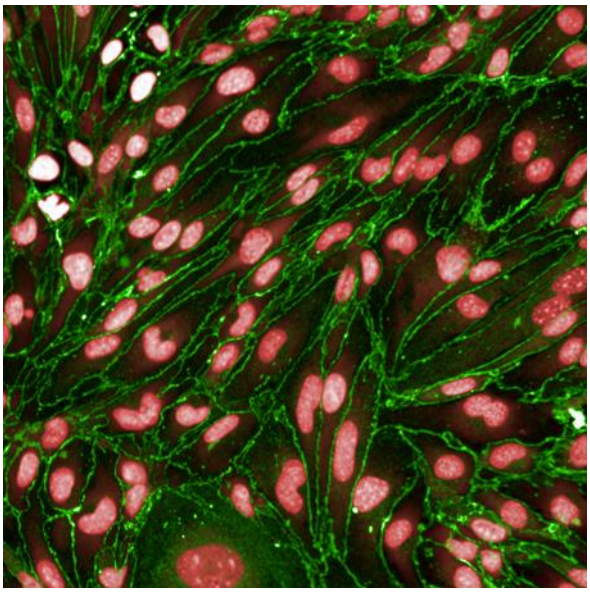

Figure 3.6: The bEnd.3 cells grown within the culture-only device were stained for ZO-1 (green) and costained with DRAQ5 (red) after 5 days of growth. By this point, the cells are highly confluent and are strongly expressing the ZO-1 TJ marker at the cell-to-cell junction, indicating a positive stain.

Improvements to the BBB Organ-on-a-Chip

Building upon the work of the first generation of the BBB organ-on-a-chip, there were several flaws with the design of the device that were used to guide the construction of the next generation of the system.

The first significant flaw was how the microcapillaries were to be modeled. To recreate the high shear stress of this environment, the experimental channels were designed to match the actual geometries of mouse microcapillaries. This led to the problem of being unable to feasibly achieve flow rates that induced the correct amount of shear stress. A flow rate of about 500 nL/min would be required to achieve 2 Pa of shear stress, which is not feasible with a peristaltic pump. *In vivo*, the mouse has a blood flow rate at the aorta of roughly 2 mL/minute.[77] However, this flow rate is divided many times over as the large blood vessels fraction off into smaller branches. By the time the blood cells of the mice reach the capillaries, the cells are traveling at a very slow flow rate. It is largely because of the small capillaries that the shear stress is so high.

The second significant flaw of the design was that the model split the single inlet channel of the device to feed both experimental and control channels. This was done to control sample variations. While controlling of sample variations is important, findings from groups such as Ulker et al. suggest that this design would not be suitable for the phenomenon that we were exploring.[78] Ulker et al. found that it was not only the induction of physiological shear stress that upregulated eNOS production, but it was also the cyclically repetitive cadence of alternating between physiologically high and low shear stress that resulted in an upregulation of eNOS activity. This phenomenon cannot be replicated in this model as the flow blood cells are only able to be introduced a single time into the device.

Additionally, this device design is limited by only integrating a single cell line. The bEnd.3 cells are widely used to model the BBB. However, this model does present with low TEER values when used in single culture. Given that in this system the primary

metric is TEER, the system has limited significance. It has been shown that when bEnd.3 cells are used in co-culture that much higher TEER values may be reached. Astrocytes are an example of a supplementary cell line that can increase the TEER of bEnd.3 cells. To incorporate astrocytes into an organ-on-a-chip system, a separation will be needed between the endothelial and astrocyte culture regions, which this design cannot accommodate.

Furthermore, the use of TEER as the primary metric of BBB integrity is a significant shortcoming of the system. A more robust system would also include permeability studies. A common marker for *in vitro* BBB permeability is for the passage of a fluorescein isothiocyanate (FITC) labeled dextran macromolecule to cross the simulated barrier into a basolateral chamber. This technique is commonly accomplished in transwell BBB models but is also implemented in more sophisticated BBB organ-on-a-chip devices. Expanding the capabilities of this device to include that secondary chamber would not only increase the impact of the design, but also allow for the culture of additional cell lines.

Lastly, the TEER system for this device was built on the two point probe method, using interdigitated electrodes.[79] While this model does provide significant information on the integrity of a biological barrier, such models are not as robust as the four point probe method. Four point probe resistance meters separate the current and voltage monitoring electrodes, and thus remove the influence of contact or probe resistance.[80] This limitation of electrode design is further exasperated with the inability to integrate this design with the previous two shortcomings of single cell line integration and the lack of a basolateral reservoir.

It was because of these reasons, that the initial proposed design of the BBB organ-on-a-chip was rejected, in lieu of a reimagined microfluidic device.

Chapter 4: The Development of the Second-Generation Blood-Brain Barrier Organ on a Chip, Micro Electrical Blood-Brain Barrier (µE-BBB)

Reimagining the BBB Organ-on-a-Chip

Similar to the first-generation of the BBB organ-on-a-chip, the second-generation of the device was also designed with Solidworks. This device is called the micro electrical blood-brain barrier (µE-BBB) and was structured to feature a luminal channel and basolateral chamber, separated by a 0.4 µm pore PC membrane (Figure 4.1). The lumen channel of the device simulated a brain microcapillary and could induce physiological levels of shear stress. The device was designed such that endothelial cells and astrocyte cells may grow within the device, and integrity of the simulated BBB may be monitored via paracellular leakage and TEER measurements.

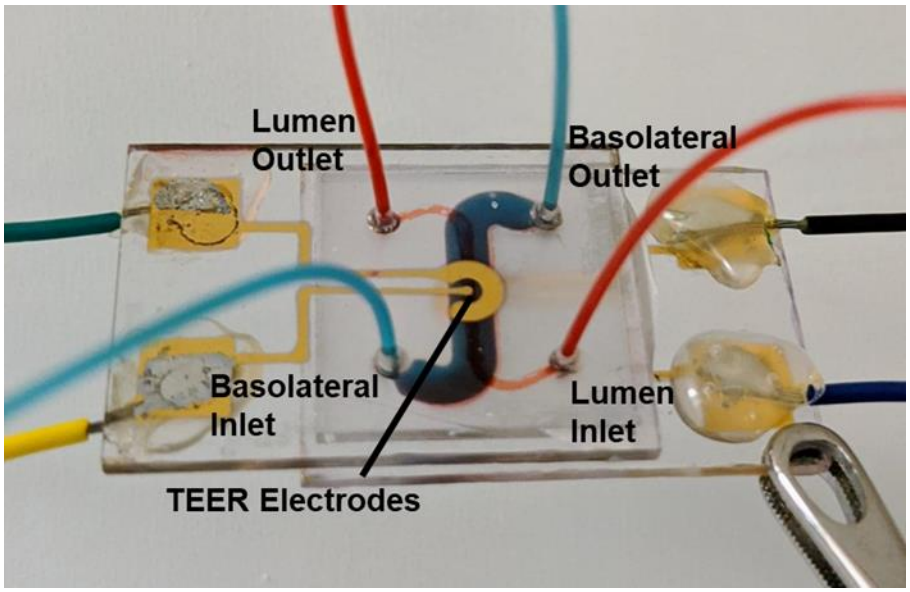

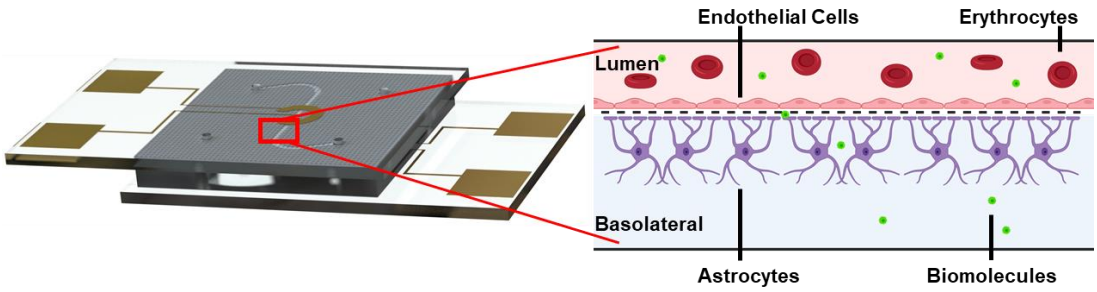

Figure 4.1: The µE-BBB consists of a lumen and basolateral chamber with integrated TEER electrodes. The chambers are separated by a porous PC membrane. The two compartments of the device allow for endothelial and astrocyte cells to grow in close proximity to each other. The barrier may be monitored through TEER measurements and through the paracellular leakage of molecules across the simulated BBB. Figure was adapted with permission from Biorender.com under a paid academic subscription.[3]

Poiseuille's equation was used to calculate the shear stress within the lumen channel.[74] The height and width of the lumen channel was 50 µm and 1 mm respectively. The cell culture media's viscosity, η, used for the µE-BBB was 1.2 mPa·s. A physiological shear stress of 2 Pa could be induced within the system when a flow rate, Q, of 40 µL/min was used in the system. Low shear stress could be induced by reducing the flow rate of the system to 8 µL/min, achieving a shear stress of 0.4 Pa.

To properly simulate the in vivo BBB, the media must be under constant flow to mimic flow within the blood vessels. However, the brain's interstitial fluid on the basolateral side of the BBB was more static. Therefore, the basolateral chamber was designed to be static and larger, amounting to 1.5 mm in height and 3 mm in width, to mimic the BBB and allow for sample collection from the chamber.

One important aspect of the design of the μE-BBB and improvement over the previous iteration of the BBB organ-on-a-chip was the layout of the TEER electrodes. These electrodes were patterned by shadow mask sputtering, and the gold deposited to a thickness of 50 nm onto precut pieces of PC stock. The strategic layout of the electrodes in relation to the cells within the μE-BBB directly affected the robust sensitivity of the system's TEER measurements. The μE-BBB was designed to be compatible with the EVOM2 epithelial voltohmmeter (World Precision Instruments) utilizing an EVOM2 Electrical Adapter (World Precision Instruments). The EVOM2 required two apical and two basolateral electrodes. The large electrodes were designated as the current electrodes, and the small electrodes were designated as voltage electrodes. The top electrode pair was connected to the I1 and V2 ports of the EVOM2 Electrical Adapter, and the bottom electrode pair was connected to the I2 and V1 ports of the EVOM2 Electrical Adapter. The electrode pairs were designed to align perpendicularly to the embedded PC membrane so that the uniform flow of ions between the electrodes minimized the noise of the system (Figure 4.2).[4] Furthermore, this system benefits from having electrodes that are fixed in place. This further prevents signal noise as there is no variation of electrode placement between measurements and the electrodes are completely static throughout the course of the acquisition. The electrodes were designed with large contact pads to allow for wire soldering connections to the EVOM2. The 22g tinned copper wires were bonded onto the gold contact pads utilizing low temperature 52In/48Tn solder, and the connections were reinforced with hot glue.

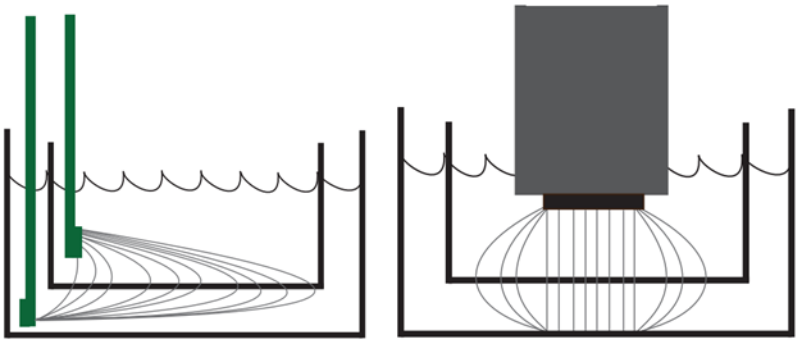

Figure 4.2: Traditional TEER electrodes do not form a uniform electric field between terminals. An advantage of the perpendicular embedded electrodes is the formation of a uniform and symmetric electric field resulting in less signal noise during measurement acquisition.[4]

Another consideration of the system was rapid, reliable fabrication. To avoid the complexity of thin, multilayer PDMS fabrication of the previous device and more traditional microfluidic devices, microfluidic tape was used instead. The microfluidic tape allowed for precise control of the thickness of the shear inducing lumen channel. The microfluidic tape had an added benefit of simplifying membrane excision for cellular imaging purposes. Exposure to isopropyl alcohol (IPA) weakens the tape's adhesive, allowing for the user to extract the embedded PC membrane.

A consideration that is made for the layout of the two chambers of the device is the cross-sectional growth area (Figure 4.3). The channels are oriented in mirrored “S” shapes, and along the center of the device the channels overlap with each other. This design element has 2 benefits. The first is the further simplification of cellular imaging, as the larger functional region results in more area that can be imaged. The second benefit is to reduce the noise that is associated with TEER measurements. TEER is normalized to

cm^2 growth area, and by increasing the value of the surface area, a smaller correction is needed to standardize the measurement.

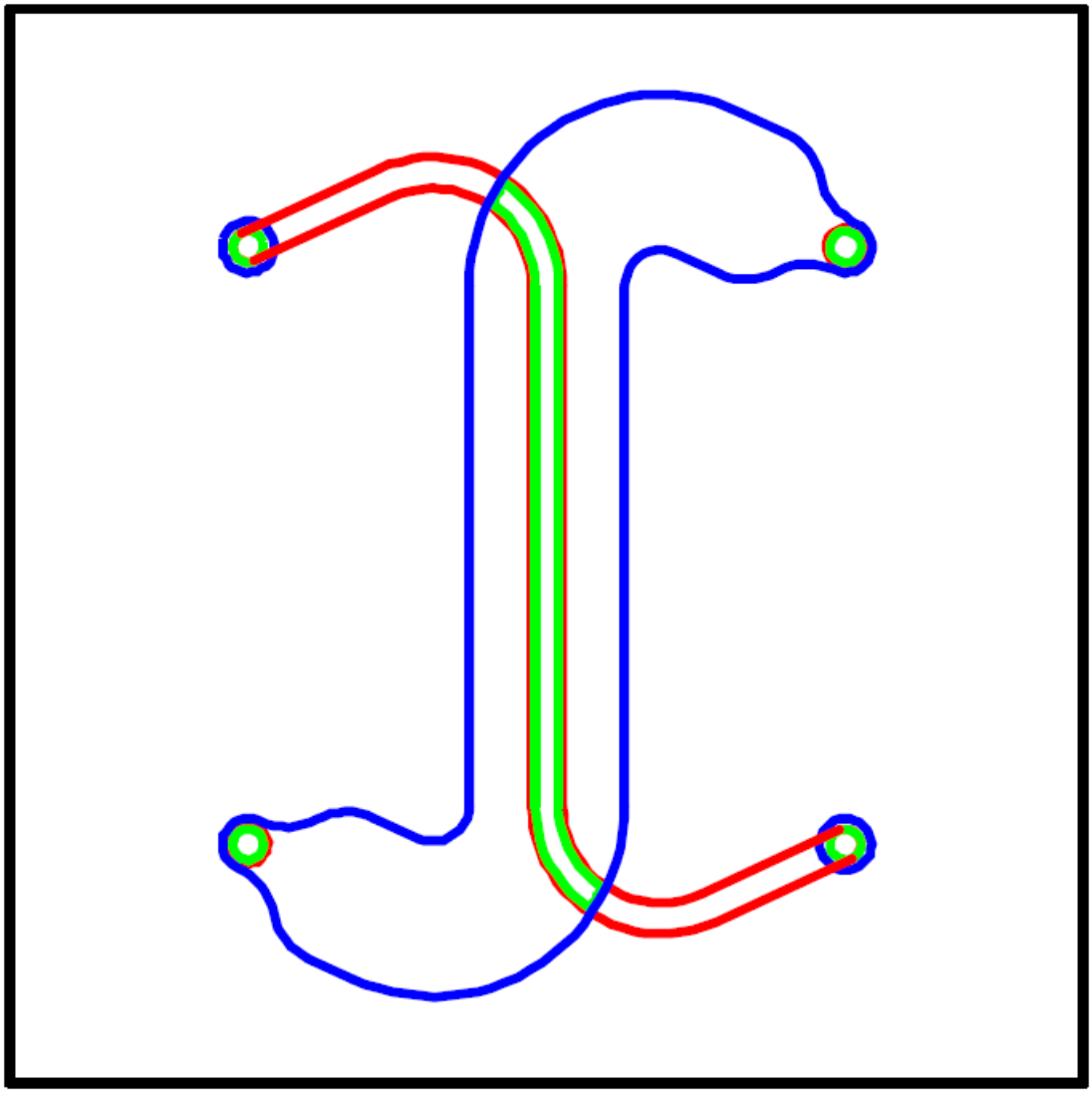

Figure 4.3: The overlayed layers correspond to the lumen profile (red), membrane-basolateral adhesive profile (green), and the basolateral profile (blue). The profiles have an elongated cross-sectional region to increase sensing area and improve microscopy visualization. The membrane basolateral adhesive profile is slightly smaller than the cross-sectional region of the lumen and basolateral profiles as a control for chip-to-chip variation.

A design element that was included in the device was the size of the membrane-basolateral adhesive layer. The opening in this layer is slightly smaller than the cross-sectional area of the basolateral chamber and the lumen channel (Figure 4.3). This consideration accounts for fabrication variation between devices. Nested within the cross-sectional area, this opening defines the boundaries (12.14 mm^2 surface area) of the fictional BBB region for the purposes of TEER normalization.

The μE-BBB assembled by adhering the subcomponents together as shown in Figure 4.4 utilizing an arbor press to compress the device and increase the strength of the pressure sensitive adhesive. The construction of the assembly can be broken into 2 parts: assembly of the membrane insert, and the assembly of the entire device. The membrane insert was fabricated by taping the circular membrane flat onto a flat substrate. The membrane-basolateral adhesive layer was lightly tacked onto the membrane in a manner that no bubbles or kinks were introduced. The assembly was then strongly compressed with the use of an arbor press. Afterwards, the membrane was detached and flipped upside down, exposing the other side of the membrane. The membrane was again taped down flat, and the lumen adhesive layer was lightly tacked onto the other side. Special care was taken to ensure that the alignment holes of the 2 adhesive layers overlapped. The membrane insert was then trimmed to size with a razor blade. Finally, the membrane that remained within the holes in the 4 corners of the insert was burned away by touching the surface with a flame-heated 22g syringe needle. The complete device was assembled with the use of an alignment jig. The alignment jig was a flat piece of stock acrylic that had holes that overlapped with the inlets and outlets of the device. Four 2 cm long sections of 22g hypodermic tubing were placed in the holes in the alignment jig and were

used as alignment guides. The µE-BBB was constructed from the top layer downward towards the bottom layer. First, the lumen electrode was placed into the alignment jig over the alignment guides, and then the membrane insert was placed onto the top layer, also following the alignment guides. The membrane insert was tacked into place, with careful attention that the lumen channel touches both current and voltage electrodes. The partial assembly was removed from the alignment jig and compressed using the arbor press. The assembly was then returned to the alignment jig, and the basolateral and basolateral adhesive layers were attached in that order. The partial assembly was then removed from the jig, and the basolateral electrode was fixed to the bottom of the device. The complete structure was then compressed again using the arbor press. PE tubing was then inserted into the inlet and outlet ports of both lumen and basolateral chambers of the device and sealed with two-part epoxy glue.

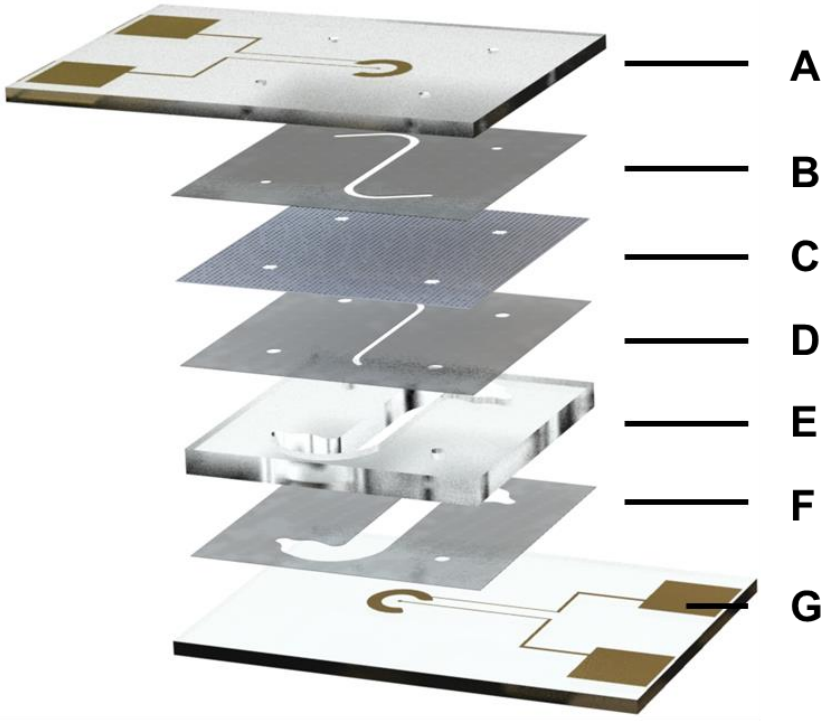

Figure 4.4: The μE-BBB is comprised of A) a lumen electrode, B) a lumen channel, C) a PC membrane, D) a membrane-basolateral adhesive layer, E) a basolateral layer, F) a basolateral electrode adhesive layer, and G) a basolateral electrode.[3]

Cell Culture Technique

Mouse brain endothelial bEnd.3 cells and mouse astrocyte C8-D1A cells (CRL-2541, American Type Culture Collection) were grown in complete growth media. The cells were grown in T-75 culture flasks and grown to 70-90% confluency. The cells were passaged with 0.25%Trypsin/0.2%EDTA and grown in a 37 °C incubator under 5% CO_2.

The μE-BBB was seeded with cells in two phases (Figure 4.5). The initial seed of astrocytes was carried out on day 0, and the seed of endothelial cells was conducted on day 2. First, the device was sterilized by flowing 70% EtOH through both channels, followed by flowing PBS. The device was then filled with 50 μg/mL fibronectin and set to incubate for 1 hour at 37 °C and subsequently filled with complete growth media and set to incubate for 2 hours at 37 °C. C8-D1A cells were introduced into the basolateral chamber at a concentration of 6e4 cells/cm^2. This was achieved by suspending the astrocytes to a concentration of 4e5 cells/mL. After seeding, the μE-BBB was placed upside down in the incubator. After 3 hours, the device was perfused with complete growth media at a rate of 0.5 μL/min. After 2 days, bEnd.3 cells were introduced to the luminal side at the same 6e4 cells/cm^2 concentration, achieved by suspending the endothelial cells to a concentration of 1.2e7 cells/mL. The device was then placed in the incubator for 3 hours to allow for cell adhesion prior to perfusing the channel at a rate of 0.5 μL/min with complete growth media. Then, the cells within the μE-BBB were

allowed to grow for an additional 5 days, to reach full maturation as monitored by TEER trendline. Maturity was initially confirmed by imaging and subsequently determined by an asymptotic TEER trendline, over 170 $\Omega \cdot cm^2$, comparable to similar models.

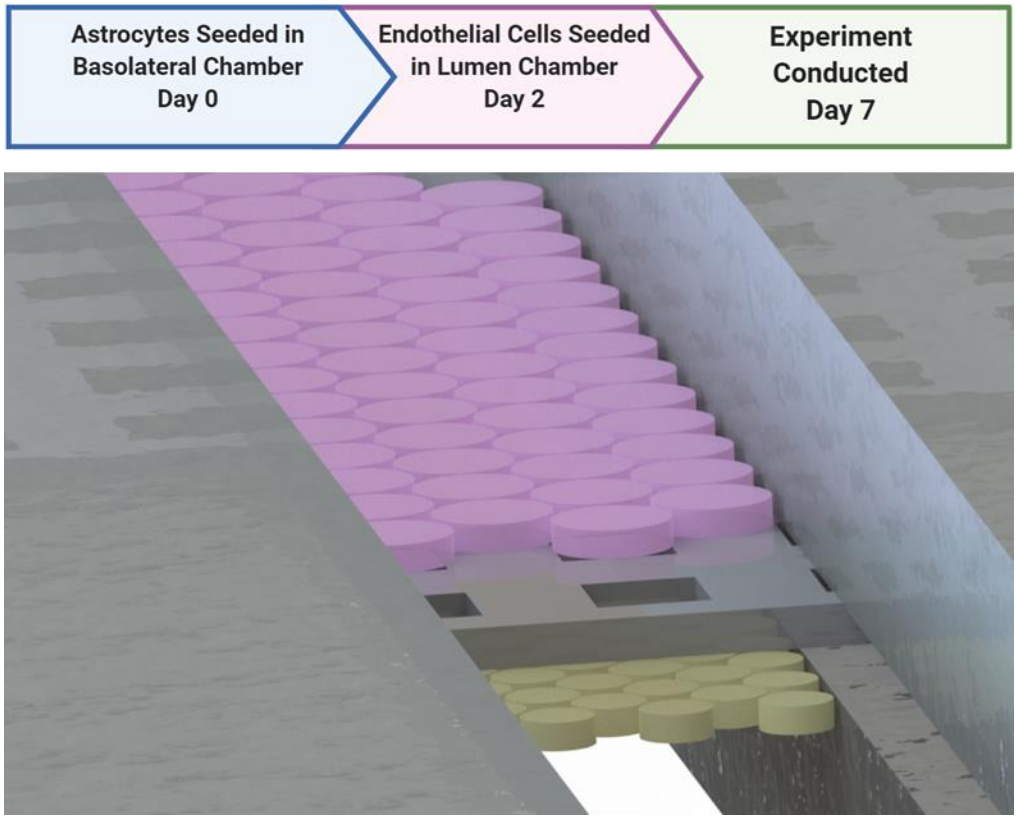

Figure 4.5: The µE-BBB is seeded with astrocytes (yellow) on day 0, and with endothelial cells (pink) on day 2. By day 7, the µE-BBB is fully mature.[3]

Simulated BBB Validation

For initial visual verification of cell growth within the µE-BBB device (Figure 4.6), H&E-stained images were collected following 7 days of growth with the C8-D1A cells and 5 days of growth with the bEnd.3 cells. This was accomplished by first incubating the cells with ice cold 4% PFA over ice for 10 minutes. The adhesive maintaining the µE-BBB was then weakened by submerging the device for 1 minute in

IPA. The membrane was then carefully excised from the µE-BBB with a razor blade, without scratching the inner growth regions of the layer. The membrane was washed 3 times with ice cold PBS, followed by a 10 minute incubation with filtered hematoxylin. After a 30 second wash with tap water, the membrane was incubated for 30 seconds with Scott's Tap Water Bluing Reagent and another 30 second wash in tap water. The membrane was then incubated for 4 minutes with Eosin Y and then a 30 second incubation with 95% EtOH. The membrane is then incubated in 100% EtOH for 2 minutes and then washed 3 times with 100% EtOH for 30 seconds per wash. The membrane was then mounted in fluoromount on a glass slide and imaged under 10x magnification.

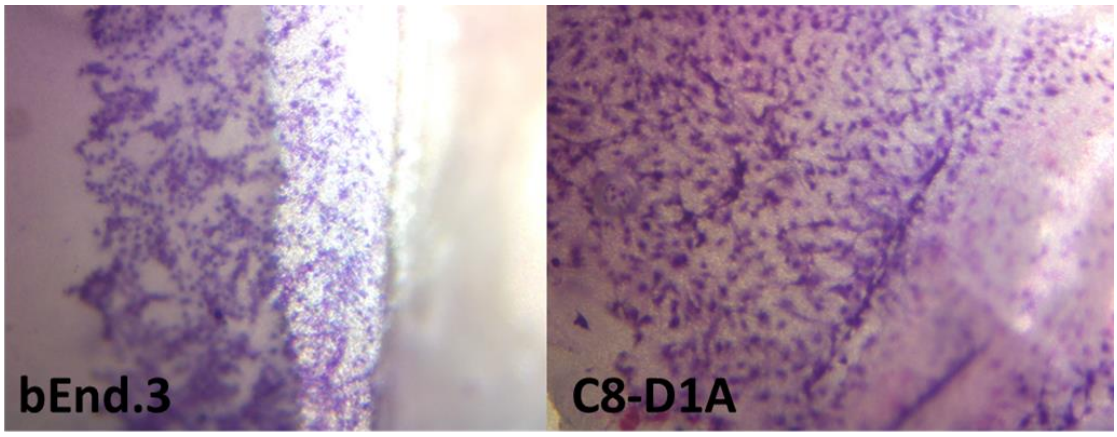

Figure 4.6: The membrane was stained for cell growth for bEnd.3 cell growth after 5 days and for C8-D1A cell growth after 7 days. Both of these conditions demonstrate that by the end of the growth period, both cell lines have formed distinct monolayers covering the membrane. The bEnd. 3 cells are visibly confined within the narrow boundary of the channel, while the C8-D1A cells extend outside the field of view of the microscope in the larger basolateral chamber.

To verify BBB normal cell growth and protein expression on the PC membrane, fluorescent images were collected of the bEnd.3 and the C8-D1A cell line (Figure 4.7). ICC staining for the cell-specific markers confirmed integration of bEnd.3 and C8-D1A cells into the device. The ICC methodology was very similar to that of the first-generation BBB organ-on-a-chip. In summary, the µE-BBB was washed with PBS and fixed with ice cold 4% PFA dissolved in PBS on ice for 15 min. The adhesive maintaining the µE-BBB was then weakened by submerging the device for 1 minute in IPA. The membrane was then excised very carefully from the µE-BBB with a razor blade. Then the membrane was precisely trimmed such that all remnants of the adhesive layers were removed, only leaving the membrane itself. Following blocking step with 5% BSA in PBS for 1 hour at room temperature, bEnd.3 cells were incubated with Alexa 488 conjugated ZO-1 or Alexa 488 conjugated claudin 5 (CLDN-5) (Invitrogen, 352588) antibodies at a 1:100 dilution in 0.75% BSA in PBS overnight at 4 °C. The C8-D1A cells were incubated with glial fibrillary acidic protein (GFAP) (Invitrogen, 13-0300) antibodies at a 1:100 dilution in 0.75% BSA in PBS overnight at 4 °C followed by a 1 hour incubation with a 488 goat anti-rat secondary (Invitrogen, A-11006) at room temperature at a 1:1000 dilution. All cells were then washed with PBS and costained with DRAQ5 at a 1:200 dilution in PBS for 30 minutes at room temperature. The membrane was mounted in fluoromount, and images were taken with the Leica SP5 Confocal Microscope.

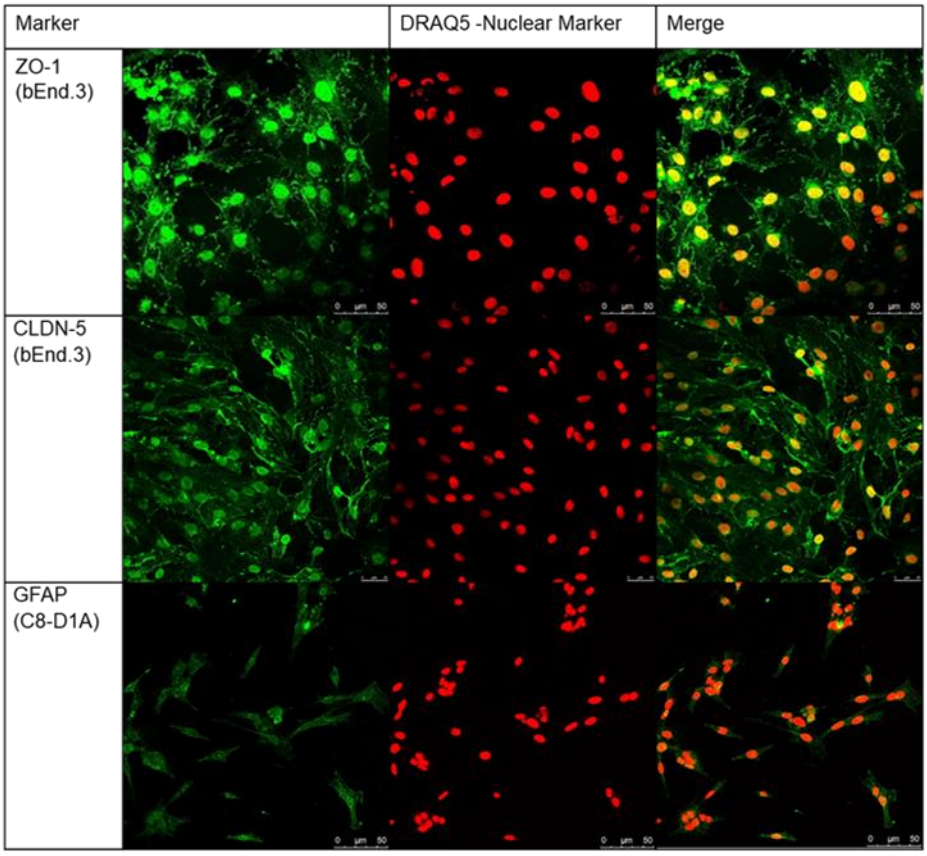

Figure 4.7: Excised membranes were stained for cell line specific markers. The bEnd.3 cells were stained for TJ markers, ZO-1 and CLDN-5, after 5 days of growth and the C8-D1A cells were stained for astrocyte marker, GFAP, after 7 days of growth. DRAQ5 was used as a nuclear costain.[3]

The endothelial bEnd.3 cells express both TJ-associated proteins, ZO-1 and CLDN-5[81] after 5 days of growth within the μE-BBB system. Specifically, the well-defined TJs are clearly identifiable with both markers. The C8-D1A astrocyte cell line, cultured on the basolateral side of the membrane, is also identifiable by its expression of GFAP.[82] Imaged after 7 days of culture, the C8-D1A cells are morphologically distinct from the bEnd.3 cells grown on the opposite surface of the embedded membrane.

These TJs play a pivotal role in establishing the barrier. However, following cell line introduction into the µE-BBB, the TJ markers are not immediately robust. Several days of cell growth are required for TJs to properly develop within the BBB.[83,84] Accordingly, we evaluated the development of the barrier over the course of 7 days by monitoring two characteristics of a functional BBB, the decreased permeability and high electrical resistance (Figure 4.8). Permeability was monitored by quantifying the accumulation of 10 kDa FITC-dextran[85,86] within the basolateral compartment of the µE-BBB after circulating a 400 µL stock of 100 µg/mL solution of FITC-dextran dissolved in phenol red-free 10 mM HEPES DMEM (blank DMEM) through the lumen of the system for 1 hour at 40 µL/min with the blood handling system developed in Chapter 2. For the experiment, the basolateral chamber of the device filled with blank DMEM. After the hour had elapsed, the circulating FITC-dextran solution, the basolateral solution, and the stock FITC-dextran (Ex. 470, Em. 514) solution was analyzed with a LightCycler 96 system (Roche). The concentrations of FITC-dextran in the lumen were calculated with the following and basolateral solutions were calculated with the fluorescence concentration equation, $[\text{Concentration}]\mu g/mL=(F_{Sample}-F_B)/(F_S-F_B)$. F_S was the fluorescence of the stock solution, F_{Sample} was the fluorescence of either the circulating lumen solution or the basolateral solution. The fluorescence of the blank media was denoted by F_B. As expected, there was no change in the permeability of FITC-dextran by day 2. This is because astrocytes alone do not provide a functional barrier.[28] However, after endothelial cells were incorporated into the device, a decrease in the basolateral accumulation of FITC-dextran was observed on days 5 ($p = 0.0286$) and 7 ($p = 0.0286$). By day 7 the permeability of the device to FITC-dextran was reduced by 24% relative to

day 0. This decrease in permeability is associated with the establishment of a tighter barrier within the system.[85,87,88]

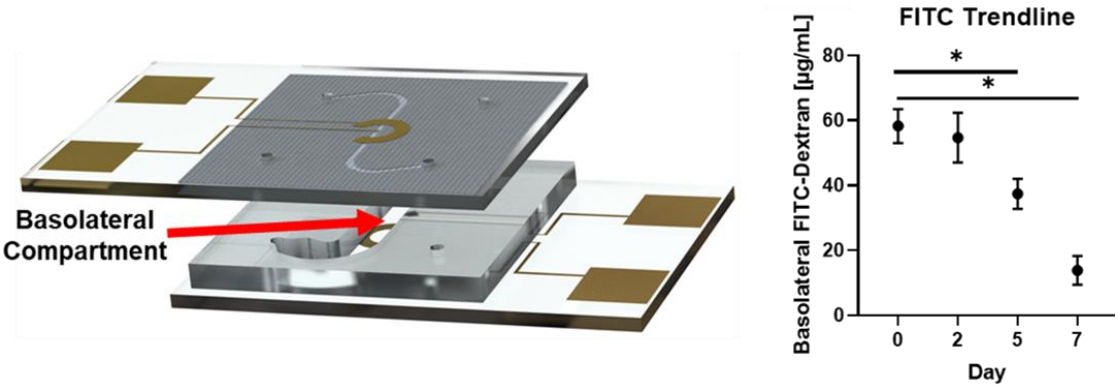

Figure 4.8: Large particle transport assays through µE-BBB were conducted by passing 100 µg mL-1 of 10 kDa FITC-dextran solution through the lumen compartment of the system for 1 hour and quantifying the amount of FITC-dextran that had accumulated in the basolateral compartment (n = 4; Mann–Whitney two-tailed test; * signifies $p < 0.05$). Initially, there is little resistance to the diffusion of FITC-dextran into the basolateral compartment, but as the device matures the permeability of the system decreases. Data represented as mean ± standard error of mean (SEM).[3]

Daily TEER measurements were collected to monitor cell growth and the validation of TJ formation (Figure 4.9). This was done utilizing an EVOM2 epithelial voltohmmeter. Alligator clips were used to connect to the EVOM2 system via an EVOM2 Electrical Adapter. The initial resistance on day 0 was collected and represented the background resistance for the system. It was observed that when the system is connected to the EVOM2, the TEER value fluctuates significantly. However, this value tends to stabilize within 30 minutes and drifts to a point of equilibrium. An average of 15

resistance readings at the point of equilibrium is used as the raw TEER value of the measurement. The corrected TEER value, as represented by the equation below, is the product of the cross-sectional growth area (12.14 mm^2) within the system and the difference of the measured resistance from the initial day 0 resistance. On-chip TEER measurements of the µE-BBB also demonstrated an increase (over 170 $\Omega \cdot cm^2$) in the electrical resistance over time after the incorporation of the endothelial cells. This is in-line with the progressive decrease in permeability and limited passage of ions across the integrated barrier after the endothelial cells are incorporated into the µE-BBB.[85,88]

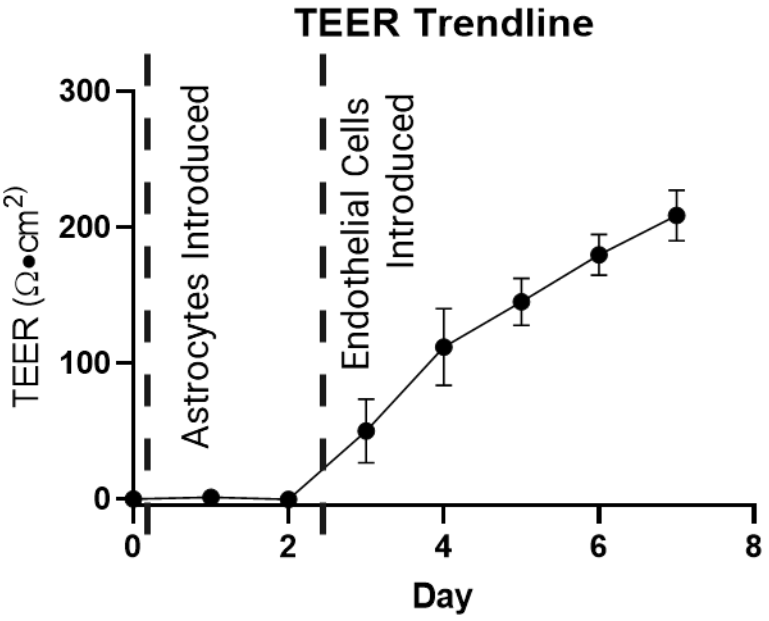

Figure 4.9: Utilizing the integrated electrodes of the system, TEER measurements were collected daily. During the first 2 days of culture, the astrocytes alone do not induce any change in resistance. However, the resistance begins to increase following incorporation of bEnd.3 cells after day 2 (n = 8). All data represented as mean ± SEM.[3]

Chapter 5: The Identification of Erythrocytes as a Contributor to Age-Associated Loss of Blood-Brain Barrier Integrity

The Effect of NO on ZO-1 TJ Expression on the Mouse BBB

NO is a molecule that increases BBB permeability.[51–54] To assess the effects of NO on TJ markers, an ICC assessment for ZO-1 was performed on endothelial cells that were exposed to the NO donor S-Nitroso-N-Acetylpenicillamine (SNAP) using staining techniques similar to those detailed in Chapter 4 (Figure 4.7).[89] SNAP is catalytically activated by trace ions present in any buffer and linearly produced NO for 6 hours after the solution is prepared. SNAP was dissolved in blank DMEM to a concentration of 1 mM. The simulated BBB was treatment with SNAP solution for 1 hour. When compared to the negative control, there was a notable decrease in the fluorescence intensity of ZO-1, indicative of decreased TJ expression (Figure 5.1).[90,91] This test showed that we were able to verify that NO does have an effect on TJ markers, and we were able to induce this effect *ex vivo* within an hour.

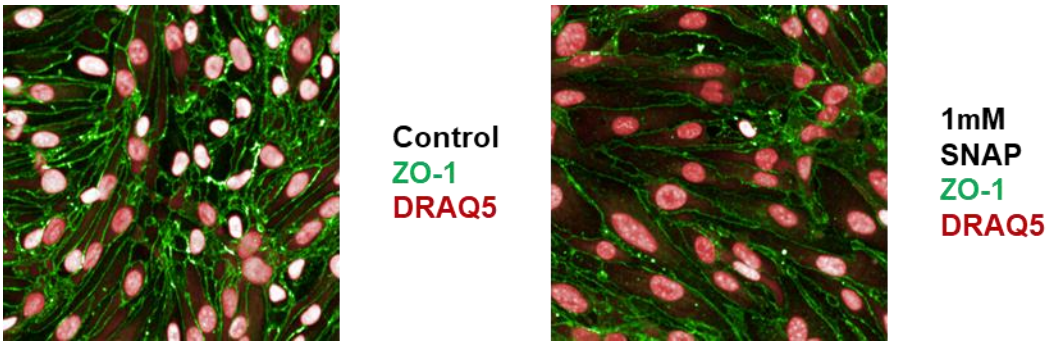

Figure 5.1: ZO-1 (green) expression was monitored after incubation with NO donor SNAP, showing a decrease in ZO-1 expression in the treated condition. DRAQ5 (red) was used as a nuclear costain.[3]

µE-BBB Analysis of NO on the Permeability of the Mouse BBB

The next goal was to evaluate the effect of NO on the permeability of the µE-BBB, using the FITC-dextran and TEER metrics employed in the Chapter 4 studies, after the administration of SNAP. A mature day 7 µE-BBB device was filled with blank DMEM and a 400 µL stock of 100 µg/mL FITC-dextran. A 1 mM SNAP solution was circulated through the lumen of the system for 1 hour at 40 µL/min with the blood handling system developed in Chapter 2. The addition of SNAP resulted in an increase in the permeability of the µE-BBB to FITC-dextran (Figure 5.2). Compared to the negative control, there was a 40% increase ($p = 0.0286$) in the accumulation of FITC-dextran in the basolateral compartment.

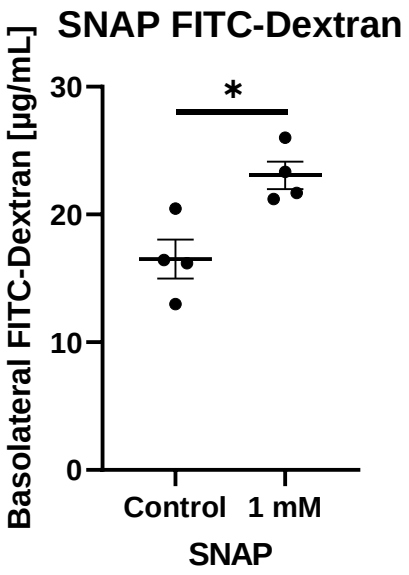

Figure 5.2: To evaluate the effect of NO on the integrity of the barrier, 1 mm SNAP and FITC-dextran were circulated through the µE-BBB. The accumulated basolateral FITC-dextran was quantified, indicating an increase in barrier permeability in the treated devices ($n = 4$).[3]

In addition, there was a 3.6% decrease in the TEER of the barrier ($p = 0.0286$) (Figure 5.3). Both of these metrics are consistent with previous studies and signify damage to the BBB.[85,87,92,93] Furthermore, this study verifies that damage to the µE-BBB is detectable and, more importantly, quantifiable.

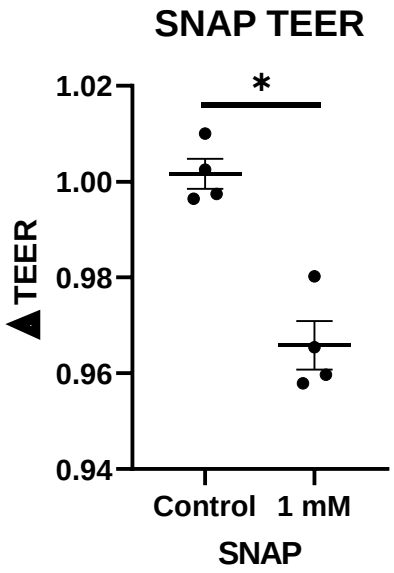

Figure 5.3: TEER evaluation of SNAP treated devices demonstrate a decrease in TEER values following the SNAP treatment, which further demonstrate damage to the µE-BBB ($n = 4$).[3]

Production of NO From Young Versus Old Mouse Erythrocytes

To confirm and extrapolate the capability of the µE-BBB system to reflect the shear induced NO production, isolated erythrocytes were passed through the lumen of a modified µE-BBB (Figure 5.4) at different flow rates (40 or 8 µL/min). Briefly, the modified µE-BBB was designed without the basolateral compartment but was still capable of inducing physiological shear stress in the lumen compartment.

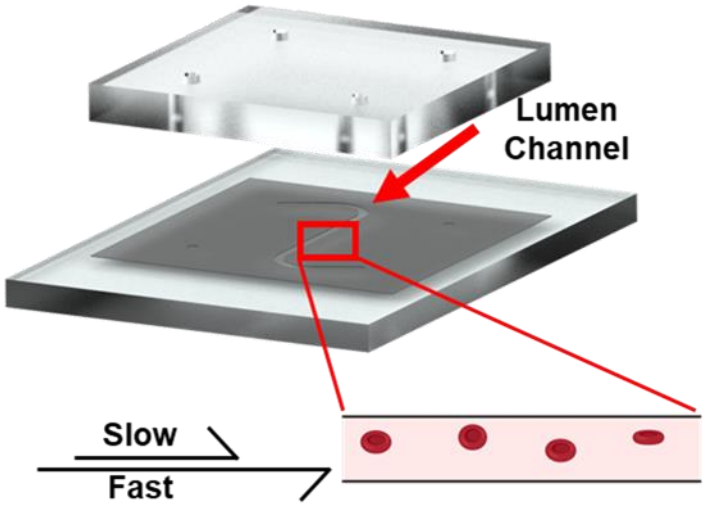

Figure 5.4: To evaluate the behavior of erythrocytes in response to shear stress, a modified µE-BBB was utilized that only contains the shear inducing lumen channel. Image was adapted with permission from Biorender.com under a paid academic subscription.[3]

The erythrocytes were derived from male C57BL/6 mice. Young mouse (2-3 months old) blood was purchased from BioIVT with sodium heparin as an anticoagulant. Old male mice (22–24 months) were purchased from the National Institute on Aging, and all animal procedures were performed in accordance with the administrative panel of the Office of Laboratory Animal Care at UC Berkeley. The protocols were approved by the UC Berkeley Animal Care and Use Committee. Blood acquired from the old mice was collected via cardiac puncture into 2-3 units of heparin per milliliter. All blood was used within 24 hours of collection.

Erythrocytes were isolated from old and young animals using Histopaque-1077. First, the blood samples were collected into a filter capped flow cytometry tube. This prevented clumping of the blood cells and removed any clots that may have formed. The

1 mL blood samples were then diluted with equal parts PBS, and carefully layered over 2 mL of Histopaque-1077. The layered solutions were then centrifuged at 400g for 30 minutes. Next the supernatant of the vial was discarded, leaving behind only the isolated erythrocytes. The cells were washed 2 times with 10 mL blank DMEM, centrifuging for 10 minutes at 250g in between, before being resuspended to a final volume of 2 mL (0.5x *in vivo* hematocrit), mixed with the NO-fluorescent probe DAF-FM,[94] and were circulated through the modified μE-BBB at low (8 μL/min) and physiological (40 μL/min) shear rates for 1 hour. The NO production was monitored fluorescently (495/515 nm excitation/absorption). Physiological shear stress did not influence the NO production of young donor erythrocytes. However, there was an increase in the old donor erythrocyte production of NO by 57% ($p = 0.0286$) (Figure 5.5). These results are in-line with the established knowledge that erythrocytes generate NO once exposed to shear stress[78] and more so that our system is capable of generating sufficient shear stress to achieve a change in production. Moreover, this also suggests that erythrocytes from young and old donors are behaving differently.

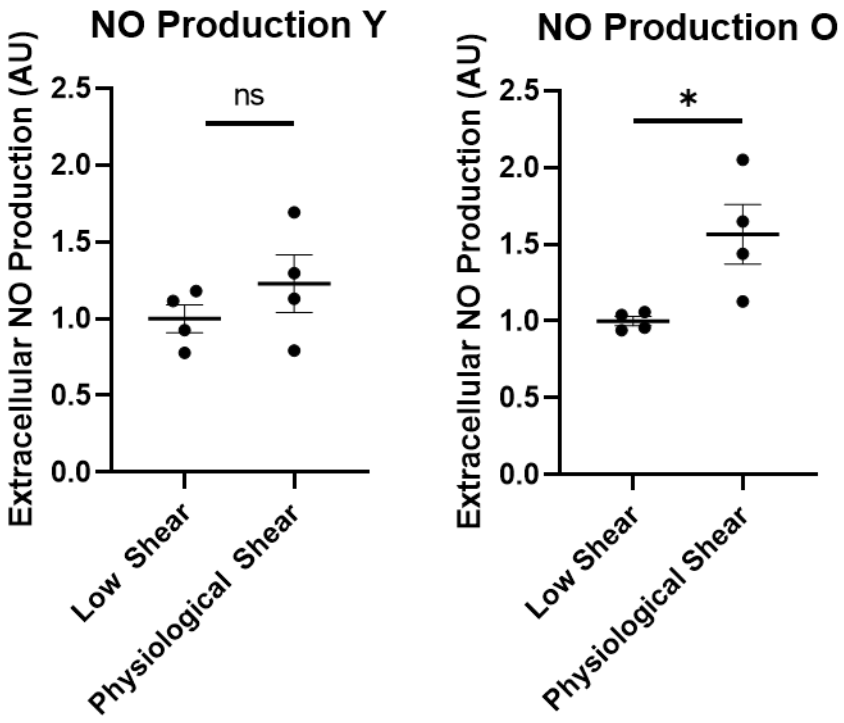

Figure 5.5: To quantify the production of NO by erythrocytes undergoing shear stress, isolated mouse erythrocytes, supplemented with NO probe DAF-FM, were circulated through the modified μE-BBB (n = 4). Under physiological shear stress conditions, there was no increase in the production of NO by young erythrocytes (n = 4). However, there was an increase in the production of NO from old mouse derived erythrocytes (n = 4). Mann–Whitney two-tailed test; ns, * signify $p > 0.05$ and $p < 0.05$, respectively. All data represented as mean ± SEM.[3]

The Effect of Old and Young Mouse Erythrocytes on the μE-BBB

Building upon these findings, the next goal was to evaluate the role of mouse erythrocytes on BBB integrity. Isolated mouse erythrocytes derived from young and old animals were circulated through the fully matured μE-BBB at low and physiological levels of shear stress. Erythrocytes from the different aged mice were resuspended to

0.5× in vivo hematocrit using the previously described protocol (without DAF-FM), but were also supplemented with 100 µg/mL 10 kDa FITC-dextran. The erythrocyte suspension was circulated through the µE-BBB for 1 hour, as described previously. Subsequently, concentrations of basolateral FITC-dextran were quantified. It was found that there were increases in basolateral FITC-dextran, suggesting a diminished µE-BBB integrity that resulted from exposing circulating erythrocytes to physiological levels of shear stress (Figure 5.6). Compared to low shear conditions, under physiological shear young animal-derived erythrocytes showed an increase in FITC-dextran permeability by 64.7% ($p = 0.0286$), while old animal-derived erythrocytes showed an almost threefold greater increase in FITC-dextran permeability, by 188.2% ($p = 0.0286$). The accumulated FITC-dextran in the basolateral chamber of the µE-BBB was 30.1% higher ($p = 0.0286$) after old animal-derived erythrocytes were circulated under physiological conditions, when compared to young animal-derived erythrocytes.

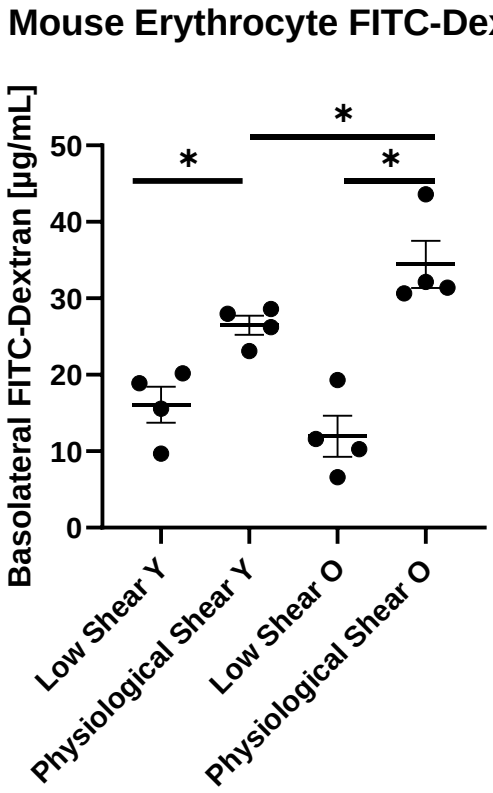

Figure 5.6: To evaluate the effect of erythrocytes on the permeability of the BBB, isolated erythrocytes from young or old mice, supplemented with FITC-dextran, were circulated through the µE-BBB. The accumulated basolateral FITC-dextran demonstrates greater barrier permeability associated with old animal derived erythrocytes under physiological conditions (n = 4). Mann–Whitney two-tailed test; * signifies $p < 0.05$. All data represented as mean ± SEM.[3]

Furthermore, TEER measurements confirmed the FITC-dextran studies (Figure 5.7). The decrease in TEER following exposure of young animal-derived erythrocytes was not significant under physiological conditions when compared to low shear conditions. Mann–Whitney two-tailed test; ns signifies $p > 0.05$. All data represented as mean ± SEM.[3]

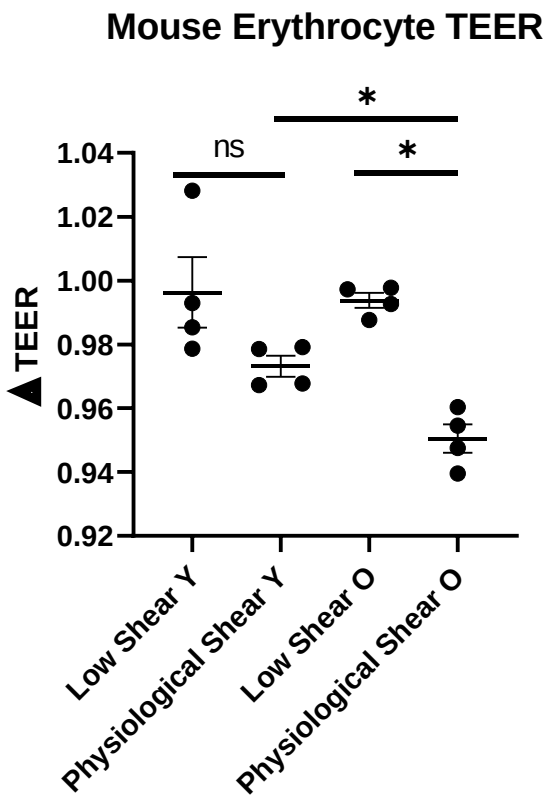

Figure 5.7: TEER analysis mirrors FITC-dextran permeability in the presence of erythrocytes from the different aged donors, demonstrating that the decrease in TEER was larger with old animal derived erythrocytes when compared to young animal derived erythrocytes under physiological conditions (n = 4). Mann–Whitney two-tailed test; ns, * signify $p > 0.05$ and $p < 0.05$, respectively. All data represented as mean ± SEM.[3]

The Quantification of Hemolysis from Isolated Human Erythrocytes from Different Age Groups

As a surrogate marker of erythrocyte integrity, free Hb was quantified following exposure to low (8 μL min−1) and physiological (40 μL min−1) levels of shear stress using the modified μE-BBB as described previously. Isolated erythrocytes from human donors were resuspended to 0.5× *in vivo* hematocrit with blank DMEM, derived from young and old human donors, following the same protocol used to isolate the mouse erythrocytes. The isolated human erythrocytes were circulated through the device and subjected to low and physiological shear stress for 1 hour. The free supernatant Hb was then quantified with spectrophotometry absorbance (520 nm absorbance).[95] Compared to low shear conditions, there was no increase in the amount of free Hb released by the young donor erythrocytes under physiological shear stress. However, there was an increase in old donor erythrocyte Hb release by 170% ($p = 0.0286$) after exposure to physiological shear stress (Figure 5.8). This lends to the hypothesis that the old donor erythrocytes are more fragile.

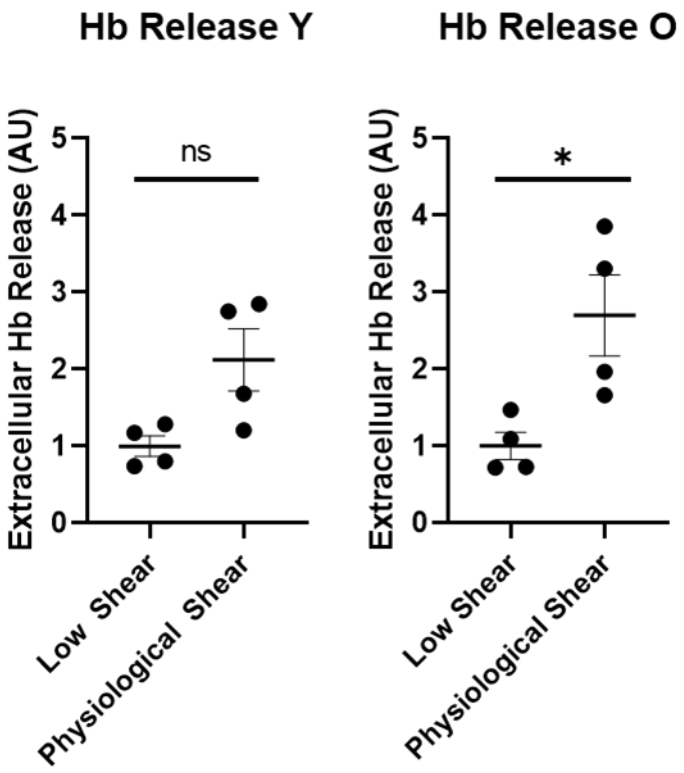

Figure 5.8: To quantify extracellular Hb, human erythrocytes were circulated through the modified μE-BBB, and supernatant 520 nm absorbance was recorded to quantify free Hb. In relation to low shear conditions, young donor erythrocytes did not release more Hb than the low shear counterparts (n = 4), but old donor erythrocytes did (n = 4). Mann–Whitney two-tailed test; ns, * signify $p > 0.05$ and $p < 0.05$, respectively. All data represented as mean ± SEM.[3]

The Effect of Shear Stress on Young and Old Human Erythrocyte Morphology

We have shown that the μE-BBB platform demonstrates the effects of old and young erythrocytes on the BBB in a mouse model. To expand this platform to the analysis of human erythrocytes, we first visualized the effect shear stress has on human erythrocyte morphology. Erythrocytes from young and old human donors were diluted to

2.5% hematocrit to allow for individual cell visualization and circulated through the modified µE-BBB system for 1 hour (Figure 5.4). Still images were captured at 0, 30, and 60 minutes (Figure 5.9). There were already more dead erythrocytes (diverging from its biconcave disk structure to an eryptosis structure),[96–98] in the old donor sample than the young donor sample before cell passage through the µE-BBB (red arrows). Circulation of erythrocytes in the µE-BBB increased the numbers of dead cells in both young and old samples; however, the rate of erythrocyte damage was greater in the old sample than in the young. Building upon the previous finding, there is now additional data supporting the theory that old donor erythrocytes are more fragile than that of younger donors.

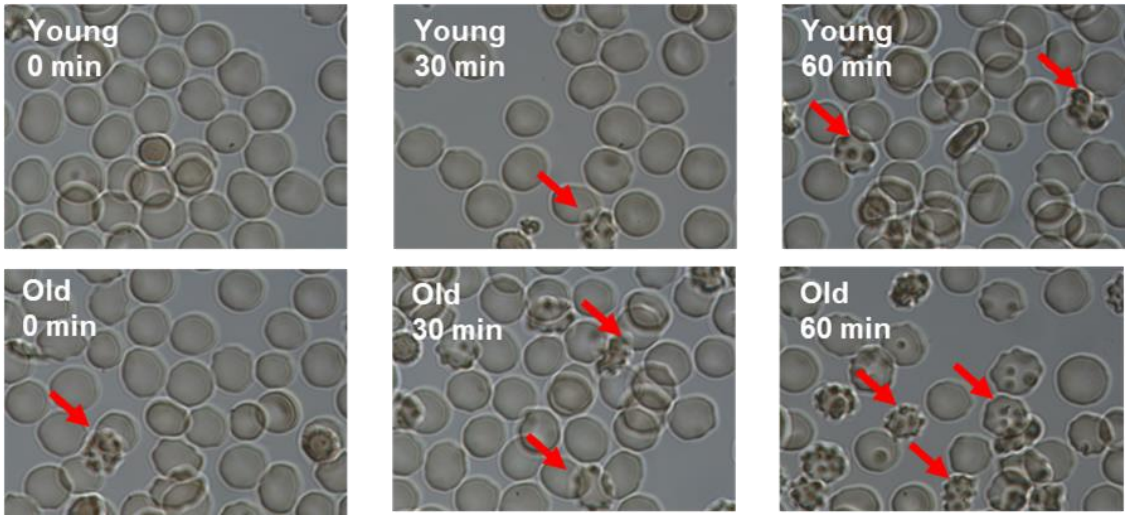

Figure 5.9: To further evaluate erythrocyte response to shear stress, young and old erythrocytes were circulated through the modified µE-BBB. After 1 hour, there was a greater prevalence of apoptotic cells in the old erythrocyte population.[3]

The Effect of Old and Young Human Erythrocytes on the µE-BBB

Previous studies used mouse cell lines in vitro, to assess the response of human cells in drug screens[99,100] and specifically cocultured human and rodent cell lines as a

BBB mimic.[101–104] In our μE-BBB, human erythrocytes were resuspended with previously described methods to 0.5× *in vivo* hematocrit and supplemented with 100 μg/mL 10 kDa FITC-dextran. The suspension was circulated through the μE-BBB for 1 hour and the concentrations of basolateral FITC-dextran were quantified. Results of this study show that when comparing old erythrocyte to young under physiological shear stress, there is an increase of 42% ($p = 0.0355$) in the μE-BBB permeability (Figure 5.10).

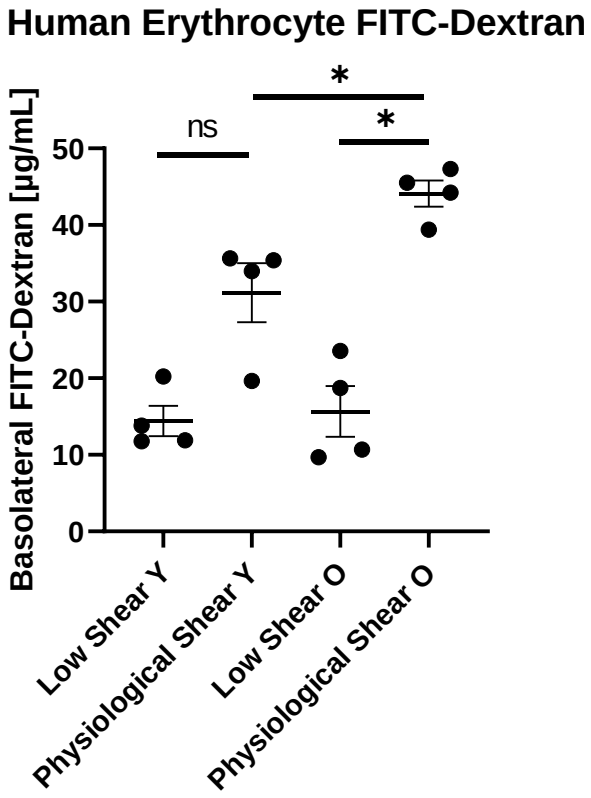

Figure 5.10: The accumulated basolateral FITC-dextran demonstrates greater barrier permeability associated with old donor erythrocytes in relation to young donor erythrocytes under physiological conditions (n = 4). Mann–Whitney two-

tailed test; ns, * signify $p > 0.05$ and $p < 0.05$, respectively. All data represented as mean ± SEM.[3]

Further corroborating this increase in permeability, a similar comparison of old to young erythrocyte circulation under physiological shear conditions was performed to assess TEER. The TEER measurements taken after circulating old human erythrocytes in µE-BBB resulted in a 2.9% larger ($p = 0.0078$) decrease in resistance when compared to young human erythrocytes (Figure 5.11). This mirrors the earlier finding with mouse derived erythrocytes. This study verifies that a similar biological phenomenon may be occurring between the mouse and human erythrocytes.

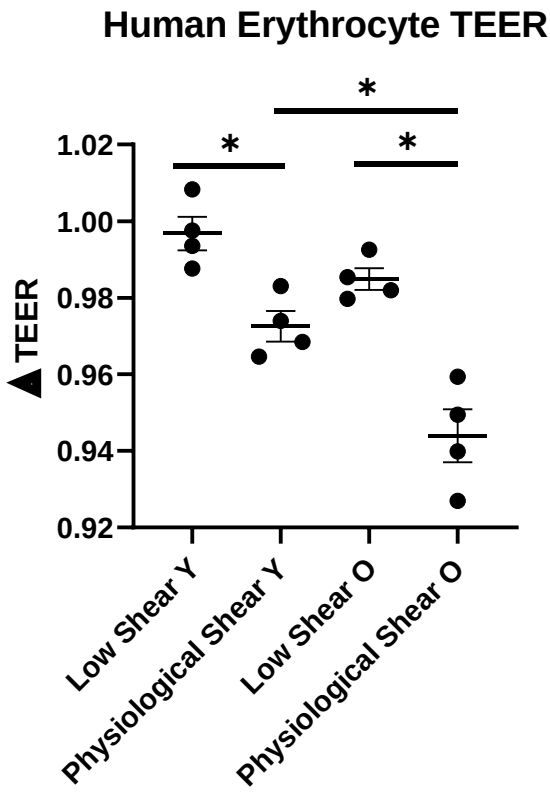

Figure 5.11: TEER analysis mirrors the trendlines of FITC-dextran permeability in the presence of human erythrocytes, with a decrease in µE-BBB electrical

resistance associated with old-derived erythrocytes when compared to young-derived erythrocytes (n = 4). Mann–Whitney two-tailed test; * signifies $p < 0.05$. All data represented as mean ± SEM.[3]

The Impact of eNOS inhibition on Old and Young Human Erythrocytes

Old donor erythrocytes have been demonstrated to produce NO at a higher rate, under physiological shear stress, than their young counterparts (Figure 5.5). This is significant because NO causes a decrease of BBB integrity (Figure 5.2, 5.3). To confirm and extrapolate the damaging effect of NO on the BBB, the μE-BBB permeability experiments were performed with erythrocytes that were exposed to the irreversible eNOS inhibitor (eNOSi) diphenyleneiodonium (DPI). Erythrocytes from young and old human donors were isolated with the Histopaque-1077 separation protocol. The only variation of this protocol was that for the last wash step, the blank DMEM was supplemented with 5 nM DPI. Following the centrifuge and decanting of the supernatant, the erythrocyte pellet was resuspended to 0.5x *in vivo* hematocrit and supplemented with 100 μg/mL 10 kDa FITC-dextran in blank media. The suspension was circulated through the μE-BBB for 1 hour and the concentrations of basolateral FITC-dextran as well as TEER were quantified. In contrast to the diminished BBB integrity when untreated old cells were circulated in μE-BBB under the physiologic shear stress (Figure 5.9, 5.10), there was no age-specific difference in BBB FITC-dextran (Fiugre 5.12) permeability or TEER (Fiugre 5.13) when donor erythrocytes were pretreated with the eNOSi, DPI.

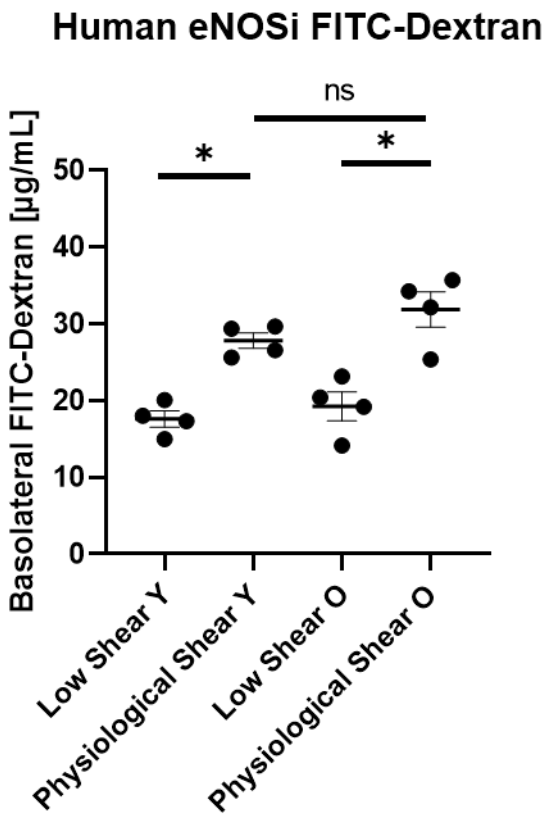

Figure 5.12: To evaluate the impact of erythrocyte produced NO on the µE-BBB, eNOSi human erythrocytes were circulated through the µE-BBB, and FITC-dextran permeability shows no difference in the effect of young and old erythrocytes on the barrier (n = 4). Mann–Whitney two-tailed test; ns, * signify $p > 0.05$ and $p < 0.05$, respectively. All data represented as mean ± SEM.[3]

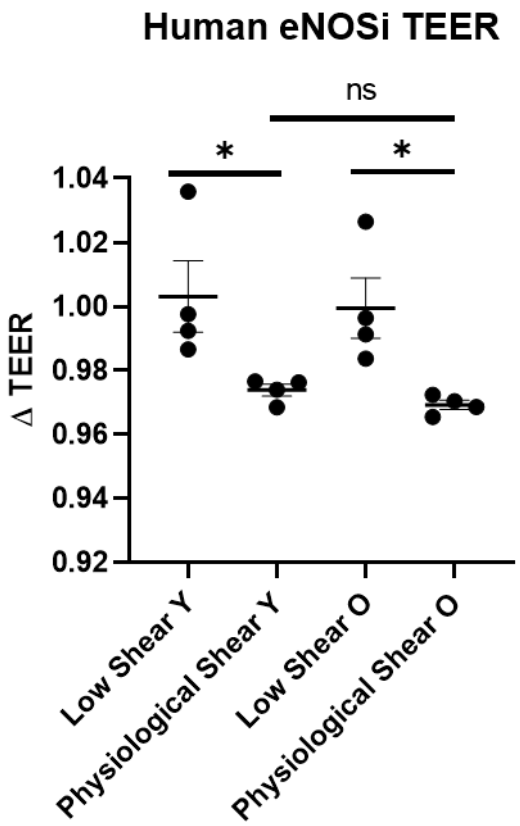

Figure 5.13: TEER analysis of eNOSi erythrocytes reaffirms the observation (n = 4). Mann–Whitney two-tailed test; ns, * signify $p > 0.05$ and $p < 0.05$, respectively. All data represented as mean ± SEM.[3]

Exploring these phenomena in more detail, DPI did not change FITC-dextran permeability with circulation of young erythrocytes in µE-BBB. However, there was a 28% decrease in FITC-dextran permeability with old erythrocytes, after treatment with DPI (Figure 5.14).

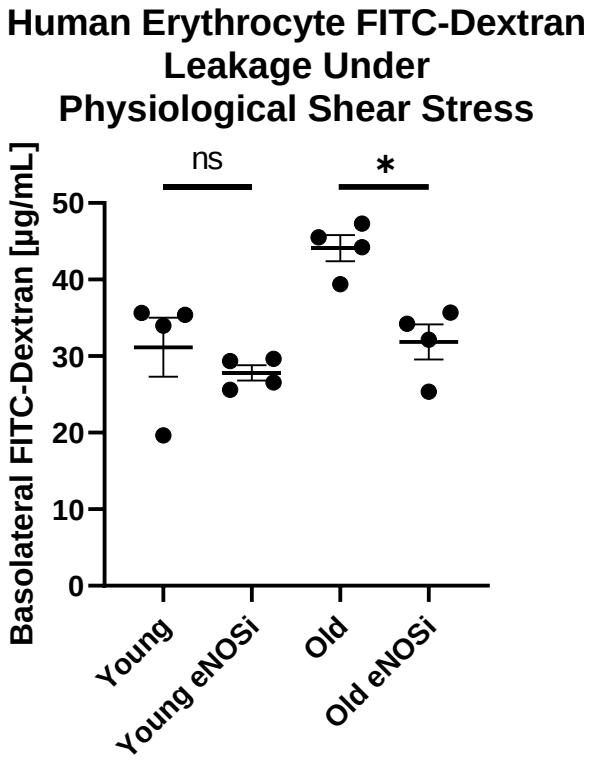

Figure 5.14: The permeability of the µE-BBB to FITC-dextran was lower in conditions where the old erythrocytes had been treated with the eNOS inhibitor, compared to the untreated sample ($n = 4$). Mann–Whitney two-tailed test; ns, * signify $p > 0.05$ and $p < 0.05$, respectively. All data represented as mean ± SEM.[3]

TEER analysis mirrored these results, with DPI having no effect of young donor erythrocytes, but resulting in a 3% smaller TEER decrease with old donor erythrocytes (Figure 5.15). This finding demonstrates the eNOS pathway as a significant contributor to age associated BBB degradation.

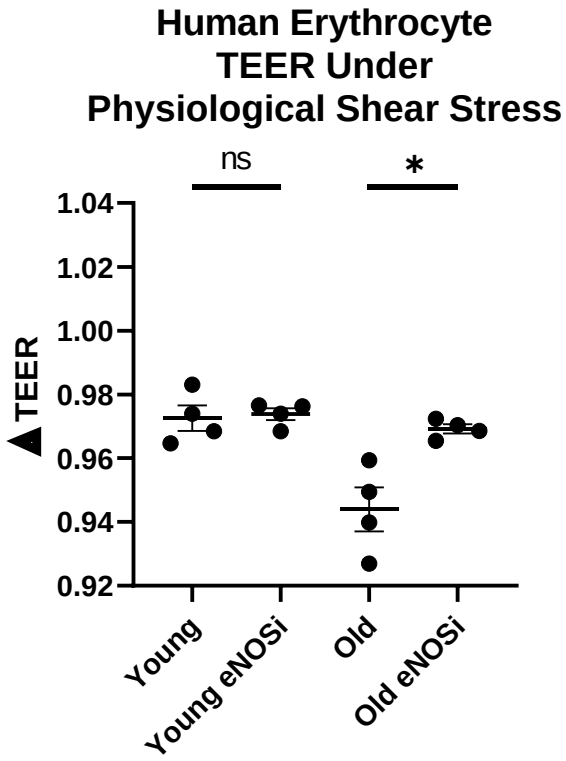

Figure 5.15: There was a smaller decrease in TEER associated with this sample set (n = 4). Mann–Whitney two-tailed test; ns, * signify $p > 0.05$ and $p < 0.05$, respectively. All data represented as mean ± SEM.[3]

Thesis Conclusion

Studies utilizing both in vivo[29,105] and ex vivo[33,85,106–110] models provided valuable information on the impact of various biomolecules on BBB, including in vivo work with calcium-binding protein B,[105] ex vivo studies with antineoplastic agent mitoxantrone,[110] and research with other chemical compounds[85,107–110] and endocrine factors.[29,105] A major challenge with these experimental systems is a lack of standardized quantification of barrier permeability under physiologically relevant parameters. This limits the potential for an accurate comparison of various factors to each other.[106,108,109,111,112] To mitigate these problems, I developed an organ-on-a-chip, the μE-BBB with built-in TEER electrodes that provides real-time feedback on BBB resistance. I have demonstrated that TEER is inversely proportional to BBB permeability, thus providing an accurate and sensitive standard quantification of barrier permeability. Furthermore, the μE-BBB can mimic the physiological flow-induced shear stress that cells experience by taking advantage of specific flow properties incorporated into its channel design.

Many factors contribute to BBB degradation, yet few are well understood in general and with respect to aging and disease. Previous studies on heterochronic blood exchange[1] and plasma manipulation[113] have established a causal connection between the age-associated hematological composition of an animal and brain health and function. In this work I demonstrate and present a novel organ-on-a chip technology which mimics physiologic circulatory changes and allows one to profile the effects of young and old environments (cells and molecules) on BBB integrity. This work demonstrates that erythrocytes are playing an essential role through their effects on the BBB. These age-specific effects are dependent on cell viability, deformability, and biochemistry, which

were all quantitatively assayed within the μE-BBB. Interestingly, dilution of old plasma with saline plus albumin improved brain health and function in mice [113,114] and attenuated progression of Alzheimer's disease in clinical trials.[115] Albumin is known to change erythrocyte aggregation and sedimentation,[116] thus it might preferentially sequester, neutralize, or buffer damaged old erythrocytes, thereby diminishing their negative effects on the BBB.

The reduction of TEER presented in this work is similar to that observed with hypoxia (9% reduction)[117] and SARS-CoV-2 infection (5% reduction),[92] although not reaching the magnitude of other pathologies like traumatic brain injury (46% reduction)[118] or ethanol usage (20% reduction).[119] Of note, the degradation of the barrier by the old erythrocytes in our system, is not akin to traumatic brain injury or hypoxia. In contrast, this is a cumulative impact of age and the most prevalent in blood cells, which in μE-BBB have detrimental effects on the barrier integrity in 1 hour.

The age-specific BBB changes are clearly due to multiple factors, and here we experimentally tested several of these. It has been hypothesized that enhanced erythrocyte eNOS activity is responsible for the degradation of the BBB. In this study, we demonstrated that NO affects TJ expression and induces BBB permeability. Furthermore, we established that old donor erythrocytes produce more NO under physiological shear stress than young. Additionally, the increase in BBB permeability by the old donor erythrocytes was reduced with eNOS inhibition. Moreover, it was hypothesized that increased fragility and higher rates of hemolysis of old erythrocytes have negative consequences for brain health,[62,63] which we confirmed and detailed for the effects on the BBB through the studies of cell morphology, cell death, and free Hb deposition.

Further research may identify erythrocytes as a target for therapy to promote healthy aging. Erythrocyte transfusions, a common FDA approved treatment for a variety of hematological conditions such as sickle cell disease or anemia, may help in improving BBB integrity. Furthermore, if erythrocyte rigidity is a cause of increased BBB permeability, therapeutics that increase erythrocyte membrane fluidity are expected to promote brain health in the old.

Technologically, this work innovates traditional models to study BBB ex vivo. The majority of systems utilize simplistic cell monolayers grown atop Transwell inserts.[120] These platforms ignore the physiological shear stress present in vivo, which is important to consider, as it is a determinant of blood and endothelial cells properties and biochemistries.[121] Additionally, our platform not only monitors the passage of various formulation across the BBB but it integrates highly sensitive electrodes across blood-brain interface to monitor TEER, as needed for accurate drug screens and for comparing candidate factors in their effects on the BBB. In commonly used TEER measurement systems, variations in the placement of the system's bulky, chopstick electrodes in-between readings present a major source of error.[4] Additionally, electrodes perpendicular to the growth area minimizes electrical noise by creating a uniform flow of ions between the electrodes. The μE-BBB with integrated perpendicular electrodes allows for reproducible real-time monitoring of barrier integrity with much better accuracy. In addition, the design and material for the μE-BBB allows rapid fabrication and are well scalable.

In regard to the microfluidic blood handling system, the custom-made technology is a powerful platform that will allow for fine manipulation of the blood composition of

mice. The programable system allows for the precise movement of biofluids in 2 directions, and the 50 µL dead space of the system allows for significant volumes (up to 250 µL) to be directed into or out of the mouse. Coupled with the predictive model, this work describes methods of bestowing more control over how much blood can be exchanged between mice and how the blood composition may be modulated for a wide scope of experiments.

Beyond age associated impacts of specific blood components, the µE-BBB can serve to monitor the effects of other hematological pathologies on the integrity of the BBB. For example, the effect of sickle cell disease on BBB integrity could be studied as well as the impact of sickle cell disease treatments. Future work will also focus on incorporating additional cell lines, such as pericytes or neurons to provide a more functional neurovascular unit. Furthermore, human cell lines can be incorporated into the system to better simulate a humanized in vivo BBB environment for a closer clinical translation, including the data on the pharmacodynamic effects of biologics. [84,120,122,123] A significant benefit of this system for pharmacodynamic studies is the standardization of the study between replicates and controls. A physiologically relevant environment is created, without the interference of *in vivo* biological redundancies or feedback loops.[124–127]

References

1. Rebo, J. *et al.* A single heterochronic blood exchange reveals rapid inhibition of multiple tissues by old blood. *Nat. Commun.* **7**, (2016).
2. Abbott, N. J., Rönnbäck, L. & Hansson, E. Astrocyte-endothelial interactions at the blood-brain barrier. *Nat. Rev. Neurosci.* **7**, 41–53 (2006).
3. Amiri, P. *et al.* Erythrocytes, a New Contributor to Age-Associated Loss of Blood-Brain Barrier Integrity. *Adv. Sci. Weinh. Baden-Wurtt. Ger.* **8**, e2101912 (2021).
4. WPI. EVOM2 Instruction Manual. https://www.wpiinc.com/media/wysiwyg/pdf/EVOM2_IM.pdf.
5. *Health, United States*. (U.S. Department of Health, Education, and Welfare, Public Health Service, Health Resources Administration, National Center for Health Statistics, 2010).
6. Farrer, L. A. *et al.* Effects of Age, Sex, and Ethnicity on the Association Between Apolipoprotein E Genotype and Alzheimer Disease: A Meta-analysis. *JAMA* **278**, 1349–1356 (1997).
7. Latourelle, J. C. *et al.* Genomewide association study for onset age in Parkinson disease. *BMC Med. Genet.* **10**, 98 (2009).
8. The Premenopausal Breast Cancer Collaborative Group. Association of Body Mass Index and Age With Subsequent Breast Cancer Risk in Premenopausal Women. *JAMA Oncol.* **4**, e181771 (2018).
9. Iversen, L. *et al.* Association between contemporary hormonal contraception and ovarian cancer in women of reproductive age in Denmark: prospective, nationwide cohort study. *BMJ* **362**, k3609 (2018).

10. Natural course of autoimmune thyroiditis in type 1 diabetes: association with gender, age, diabetes duration, and puberty | Archives of Disease in Childhood. https://adc.bmj.com/content/90/4/411.short.

11. Volkow, N. D. *et al.* Association Between Age-Related Decline in Brain Dopamine Activity and Impairment in Frontal and Cingulate Metabolism. *Am. J. Psychiatry* **157**, 75–80 (2000).

12. HYATT, R. H., WHITELAW, M. N., BHAT, A., SCOTT, S. & MAXWELL, J. D. Association of Muscle Strength with Functional Status of Elderly People. *Age Ageing* **19**, 330–336 (1990).

13. Ray, J., Popli, G. & Fell, G. Association of Cognition and Age-Related Hearing Impairment in the English Longitudinal Study of Ageing. *JAMA Otolaryngol. Neck Surg.* **144**, 876–882 (2018).

14. Oh, H., Madison, C., Villeneuve, S., Markley, C. & Jagust, W. J. Association of Gray Matter Atrophy with Age, β-Amyloid, and Cognition in Aging. *Cereb. Cortex* **24**, 1609–1618 (2014).

15. Dik, M. G., Deeg, D. J. H., Visser, M. & Jonker, C. Early Life Physical Activity and Cognition at Old Age. *J. Clin. Exp. Neuropsychol.* **25**, 643–653 (2003).

16. Nutritional aspects of cardiovascular disease. Report of the Cardiovascular Review Group Committee on Medical Aspects of Food Policy. *Rep. Health Soc. Subj. (Lond.)* **46**, 1–186 (1994).

17. Finerty, J. C., Binhammer, R. & Schneider, M. Protection of irradiated rats by parabiosis. *Tex. Rep. Biol. Med.* **10**, 496–500 (1952).

18. Hall, C. E., Hall, O. & Nevis, A. H. Prolongation of survival by parabiosis in strain 129 dystrophic mice. *Am. J. Physiol.* **196**, 110–112 (1959).

19. Conboy, I. M. *et al.* Rejuvenation of aged progenitor cells by exposure to a young systemic environment. *Nature* **433**, 760–764 (2005).

20. Conboy, I. M., Conboy, M. J. & Rebo, J. Systemic Problems: A perspective on stem cell aging and rejuvenation. *Aging* **7**, 754–765 (2015).

21. Conboy, I. M. & Rando, T. A. Heterochronic parabiosis for the study of the effects of aging on stem cells and their niches. *Cell Cycle Georget. Tex* **11**, 2260–2267 (2012).

22. Schaffer, D. V. & Gage, F. H. Neurogenesis and neuroadaptation. *Neuromolecular Med.* **5**, 1–9 (2004).

23. Bruel-Jungerman, E., Laroche, S. & Rampon, C. New neurons in the dentate gyrus are involved in the expression of enhanced long-term memory following environmental enrichment. *Eur. J. Neurosci.* **21**, 513–521 (2005).

24. Pardridge, W. M., Oldendorf, W. H., Cancilla, P. & Frank, H. J. Blood-brain barrier: interface between internal medicine and the brain. *Ann. Intern. Med.* **105**, 82–95 (1986).

25. Zlokovic, B. V. The blood-brain barrier in health and chronic neurodegenerative disorders. *Neuron* **57**, 178–201 (2008).

26. Davalos, D. *et al.* Fibrinogen-induced perivascular microglial clustering is required for the development of axonal damage in neuroinflammation. *Nat. Commun.* **3**, 1227 (2012).

27. Yousef, H. *et al.* Systemic attenuation of the TGF-β pathway by a single drug simultaneously rejuvenates hippocampal neurogenesis and myogenesis in the same old mammal. *Oncotarget* **6**, 11959–11978 (2015).

28. Riesen, F. K., Rothen-Rutishauser, B. & Wunderli-Allenspach, H. A ZO1-GFP fusion protein to study the dynamics of tight junctions in living cells. *Histochem. Cell Biol.* **117**, 307–315 (2002).

29. Bell, R. D. *et al.* Pericytes control key neurovascular functions and neuronal phenotype in the adult brain and during brain aging. *Neuron* **68**, 409–427 (2010).

30. Bailey, T. L., Rivara, C. B., Rocher, A. B. & Hof, P. R. The nature and effects of cortical microvascular pathology in aging and Alzheimer's disease. *Neurol. Res.* **26**, 573–578 (2004).

31. van de Haar, H. J. *et al.* Blood-Brain Barrier Leakage in Patients with Early Alzheimer Disease. *Radiology* **281**, 527–535 (2016).

32. Minagar, A. & Alexander, J. S. Blood-brain barrier disruption in multiple sclerosis. *Mult. Scler. J.* **9**, 540–549 (2003).

33. Qin, X. *et al.* Apolipoprotein E Mimetic Peptide Increases Cerebral Glucose Uptake by Reducing Blood-Brain Barrier Disruption after Controlled Cortical Impact in Mice: An 18F-Fluorodeoxyglucose PET/CT Study. *J. Neurotrauma* **34**, 943–951 (2017).

34. Dean, L. *Blood and the cells it contains*. *Blood Groups and Red Cell Antigens [Internet]* (National Center for Biotechnology Information (US), 2005).

35. Doyle, L. M. & Wang, M. Z. Overview of Extracellular Vesicles, Their Origin, Composition, Purpose, and Methods for Exosome Isolation and Analysis. *Cells* **8**, 727 (2019).

36. Mathew, J., Sankar, P. & Varacallo, M. Physiology, Blood Plasma. in *StatPearls* (StatPearls Publishing, 2021).

37. Minchin, S. & Lodge, J. Understanding biochemistry: structure and function of nucleic acids. *Essays Biochem.* **63**, 433–456 (2019).

38. Chanutin, A. & Curnish, R. R. Effect of organic and inorganic phosphates on the oxygen equilibrium of human erythrocytes. *Arch. Biochem. Biophys.* **121**, 96–102 (1967).

39. Thiagarajan, P., Parker, C. J. & Prchal, J. T. How Do Red Blood Cells Die? *Front. Physiol.* **12**, 318 (2021).

40. Piomelli, S. & Seaman, C. Mechanism of red blood cell aging: relationship of cell density and cell age. *Am. J. Hematol.* **42**, 46–52 (1993).

41. Horký, J., Vácha, J. & Znojil, V. Comparison of life span of erythrocytes in some inbred strains of mouse using 14C-labelled glycine. *Physiol. Bohemoslov.* **27**, 209–217 (1978).

42. Goodman, J. W. & Smith, L. H. Erythrocyte life span in normal mice and in radiation bone marrow chimeras. *Am. J. Physiol.* **200**, 764–770 (1961).

43. Abe, H., Orita, M. & Arichi, S. Erythrocyte deformability in aging. *Mech. Ageing Dev.* **27**, 383–390 (1984).

44. Franzini, E. *et al.* The role of red cells subpopulations in the determination of erythrocyte deformability. *Clin. Hemorheol. Microcirc.* **8**, 493–499 (2016).

45. Tozzi-Ciancarelli, M. G. *et al.* Age-dependent changes in human erythrocyte properties. *Clin. Hemorheol. Microcirc.* **9**, 999–1007 (2016).

46. Rifkind, J. M. *et al.* Maze learning impairment is associated with stress hemopoiesis induced by chronic treatment of aged rats with human recombinant erythropoietin. *Life Sci.* **64**, 237–247 (1998).

47. Wahnon, R., Mokady, S. & Cogan, U. Age and membrane fluidity. *Mech. Ageing Dev.* **50**, 249–255 (1989).

48. Dupire, J., Socol, M. & Viallat, A. Full dynamics of a red blood cell in shear flow. *Proc. Natl. Acad. Sci. U. S. A.* **109**, 20808–20813 (2012).

49. Cortese-Krott, M. M. & Kelm, M. Endothelial nitric oxide synthase in red blood cells: key to a new erythrocrine function? *Redox Biol.* **2**, 251–258 (2014).

50. Ulker, P., Sati, L., Celik-Ozenci, C., Meiselman, H. J. & Baskurt, O. K. Mechanical stimulation of nitric oxide synthesizing mechanisms in erythrocytes. *Biorheology* **46**, 121–132 (2009).

51. Olivera, G. C. *et al.* Nitric Oxide Protects against Infection-Induced Neuroinflammation by Preserving the Stability of the Blood-Brain Barrier. *PLoS Pathog.* **12**, (2016).

52. Shukla, A., Dikshit, M. & Srimal, R. C. Nitric oxide-dependent blood-brain barrier permeability alteration in the rat brain. *Experientia* **52**, 136–140 (1996).

53. Weyerbrock, A., Walbridge, S., Saavedra, J. E., Keefer, L. K. & Oldfield, E. H. Differential effects of nitric oxide on blood–brain barrier integrity and cerebral blood flow in intracerebral C6 gliomas. *Neuro-Oncol.* **13**, 203–211 (2011).

54. Janigro, D., West, G. A., Nguyen, T. S. & Winn, H. R. Regulation of blood-brain barrier endothelial cells by nitric oxide. *Circ. Res.* **75**, 528–538 (1994).

55. Tasdemiroglu, E., Christenberry, P. D., Ardell, J. L., Chronister, R. B. & Taylor, A. E. Effects of antioxidants on the blood-brain barrier and postischemic hyperemia. *Acta Neurochir. (Wien)* **131**, 302–309 (1994).

56. Lee, B. K., Hyun, S.-W. & Jung, Y.-S. Yuzu and Hesperidin Ameliorate Blood-Brain Barrier Disruption during Hypoxia via Antioxidant Activity. *Antioxid. Basel Switz.* **9**, (2020).

57. Bizjak, D. A. *et al.* Does endurance training improve red blood cell aging and hemorheology in moderate-trained healthy individuals? *J. Sport Health Sci.* **9**, 595–603 (2020).

58. Ward, K. A., Baker, C., Roebuck, L., Wickline, K. & Schwartz, R. W. Red blood cell deformability: Effect of age and smoking. *AGE* **14**, 73 (1991).

59. Magnani, M. *et al.* Effect of age on some properties of mice erythrocytes. *Mech. Ageing Dev.* **42**, 37–47 (1988).

60. Pinkofsky, H. B. The effect of donor age on human erythrocyte density distribution. *Mech. Ageing Dev.* **97**, 73–79 (1997).

61. Glass, G. A., Gershon, D. & Gershon, H. Some characteristics of the human erythrocyte as a function of donor and cell age. *Exp. Hematol.* **13**, 1122–1126 (1985).

62. Butt, O. I., Buehler, P. W. & D'Agnillo, F. Blood-Brain Barrier Disruption and Oxidative Stress in Guinea Pig after Systemic Exposure to Modified Cell-Free Hemoglobin. *Am. J. Pathol.* **178**, 1316–1328 (2011).

63. Ware, K. M. *et al.* The Severity of Intracranial Hemorrhages Measured by Free Hemoglobin in the Brain Depends on the Anticoagulant Class: Experimental Data. *Stroke Res. Treat.* **2017**, (2017).

64. National Centre fro the Replacement Refienment & Reduction of Animals in Research. Mouse : Decision tree for blood sampling | NC3Rs.

65. Drucker, D. J. The role of gut hormones in glucose homeostasis. *J. Clin. Invest.* **117**, 24–32 (2007).

66. Chidakel, A., Mentuccia, D. & Celi, F. s. Peripheral Metabolism of Thyroid Hormone and Glucose Homeostasis. *Thyroid* **15**, 899–903 (2005).

67. Norris, J. M. & Rich, S. S. Genetics of Glucose Homeostasis. *Arterioscler. Thromb. Vasc. Biol.* **32**, 2091–2096 (2012).

68. Esser, F., Masselter, T. & Speck, T. Silent Pumpers: A Comparative Topical Overview of the Peristaltic Pumping Principle in Living Nature, Engineering, and Biomimetics. *Adv. Intell. Syst.* **1**, 1900009 (2019).

69. Li, Z., Yi Mak, S., Sauret, A. & Cheung Shum, H. Syringe-pump-induced fluctuation in all-aqueous microfluidic system implications for flow rate accuracy. *Lab. Chip* **14**, 744–749 (2014).

70. Cabuz, C., Herb, W. R., Cabuz, E. I. & Lu, S. T. The dual diaphragm pump. in *Technical Digest. MEMS 2001. 14th IEEE International Conference on Micro Electro Mechanical Systems (Cat. No.01CH37090)* 519–522 (2001). doi:10.1109/MEMSYS.2001.906593.

71. Nosé, Y. Design and Development Strategy for the Rotary Blood Pump. *Artif. Organs* **22**, 438–446 (1998).

72. Badamasi, Y. A. The working principle of an Arduino. in *2014 11th International Conference on Electronics, Computer and Computation (ICECCO)* 1–4 (2014). doi:10.1109/ICECCO.2014.6997578.

73. Warren, J.-D., Adams, J. & Molle, H. Arduino for Robotics. in *Arduino Robotics* (eds. Warren, J.-D., Adams, J. & Molle, H.) 51–82 (Apress, 2011). doi:10.1007/978-1-4302-3184-4_2.

74. Zheng, X. & Silber-Li, Z. Measurement of velocity profiles in a rectangular microchannel with aspect ratio α = 0.35. *Exp. Fluids* **44**, 951–959 (2008).

75. Zhang, W. Y., Ferguson, G. S. & Tatic-Lucic, S. Elastomer-supported cold welding for room temperature wafer-level bonding. in *17th IEEE International Conference on Micro Electro Mechanical Systems. Maastricht MEMS 2004 Technical Digest* 741–744 (2004). doi:10.1109/MEMS.2004.1290691.

76. Ghaemi, R. *et al. A UNIVERSAL METHOD TO BOND SILICONES TO POLYMERIC AND METALLIC SUBSTRATES*. (2017).

77. Xie, C., Wei, W., Zhang, T., Dirsch, O. & Dahmen, U. Monitoring of Systemic and Hepatic Hemodynamic Parameters in Mice. *J. Vis. Exp. JoVE* 51955 (2014) doi:10.3791/51955.

78. Ulker, P. *et al.* Shear stress activation of nitric oxide synthase and increased nitric oxide levels in human red blood cells. *Nitric Oxide Biol. Chem. Off. J. Nitric Oxide Soc.* **24**, 184–191 (2011).

79. Schmiedinger, T. *et al.* Interdigitated aluminium and titanium sensors for assessing epithelial barrier functionality by electric cell-substrate impedance spectroscopy (ECIS). *Biomed. Microdevices* **22**, 30 (2020).

80. Elbrecht, D. H. & Hickman, C. J. L. and J. J. Transepithelial/endothelial Electrical Resistance (TEER) theory and applications for microfluidic body-on-a-chip devices. *J. Rare Dis. Res. Treat.* **1**, (2016).

81. Jiao, H., Wang, Z., Liu, Y., Wang, P. & Xue, Y. Specific Role of Tight Junction Proteins Claudin-5, Occludin, and ZO-1 of the Blood–Brain Barrier in a Focal Cerebral Ischemic Insult. *J. Mol. Neurosci.* **44**, 130–139 (2011).

82. Hol, E. M. & Pekny, M. Glial fibrillary acidic protein (GFAP) and the astrocyte intermediate filament system in diseases of the central nervous system. *Curr. Opin. Cell Biol.* **32**, 121–130 (2015).

83. Kim, J. A. *et al.* Collagen-based brain microvasculature model in vitro using three-dimensional printed template. *Biomicrofluidics* **9**, 024115 (2015).

84. He, F. *et al.* [Immortalized mouse brain endothelial cell line Bend.3 displays the comparative barrier characteristics as the primary brain microvascular endothelial cells]. *Zhongguo Dang Dai Er Ke Za Zhi Chin. J. Contemp. Pediatr.* **12**, 474–478 (2010).

85. Booth, R. & Kim, H. Characterization of a microfluidic in vitro model of the blood-brain barrier (μBBB). *Lab. Chip* **12**, 1784–1792 (2012).

86. Kumar, M. & Nerurkar, V. R. In Vitro and In Vivo Blood–Brain Barrier Models to Study West Nile Virus Pathogenesis. *Methods Mol. Biol. Clifton NJ* **1435**, 103–113 (2016).

87. Booth, R. & Kim, H. Permeability analysis of neuroactive drugs through a dynamic microfluidic in vitro blood-brain barrier model. *Ann. Biomed. Eng.* **42**, 2379–2391 (2014).

88. Ahn, S. I. *et al.* Microengineered human blood–brain barrier platform for understanding nanoparticle transport mechanisms. *Nat. Commun.* **11**, 175 (2020).

89. Feelisch, M. The Biochemical Pathways of Nitric Oxide Formation from Nitrovasodilators: Appropriate Choice of Exogenous NO Donors and Aspects of Preparation and Handling of Aqueous NO Solutions. *J. Cardiovasc. Pharmacol.* **17**, S25 (1991).

90. Maiers, J. L., Peng, X., Fanning, A. S. & DeMali, K. A. ZO-1 recruitment to α-catenin – a novel mechanism for coupling the assembly of tight junctions to adherens junctions. *J. Cell Sci.* **126**, 3904–3915 (2013).

91. Rodgers, L. S., Beam, M. T., Anderson, J. M. & Fanning, A. S. Epithelial barrier assembly requires coordinated activity of multiple domains of the tight junction protein ZO-1. *J. Cell Sci.* **126**, 1565–1575 (2013).

92. Buzhdygan, T. P. *et al.* The SARS-CoV-2 spike protein alters barrier function in 2D static and 3D microfluidic in-vitro models of the human blood–brain barrier. *Neurobiol. Dis.* **146**, 105131 (2020).

93. Haorah, J., Knipe, B., Gorantla, S., Zheng, J. & Persidsky, Y. Alcohol-induced blood-brain barrier dysfunction is mediated via inositol 1,4,5-triphosphate receptor (IP3R)-gated intracellular calcium release. *J. Neurochem.* **100**, 324–336 (2007).

94. Kojima, H., Hirata, M., Kudo, Y., Kikuchi, K. & Nagano, T. Visualization of oxygen-concentration-dependent production of nitric oxide in rat hippocampal slices during aglycemia. *J. Neurochem.* **76**, 1404–1410 (2001).

95. Taparia, N., Platten, K. C., Anderson, K. B. & Sniadecki, N. J. A microfluidic approach for hemoglobin detection in whole blood. *AIP Adv.* **7**, 105102 (2017).

96. Pyrshev, K. A., Klymchenko, A. S., Csúcs, G. & Demchenko, A. P. Apoptosis and eryptosis: Striking differences on biomembrane level. *Biochim. Biophys. Acta BBA - Biomembr.* **1860**, 1362–1371 (2018).

97. Bratosin, D. *et al.* On the evolution of erythrocyte programmed cell death: apoptosis of Rana esculenta nucleated red blood cells involves cysteine proteinase activation and mitochondrion permeabilization. *Biochimie* **86**, 183–192 (2004).

98. Bratosin, D. *et al.* Programmed cell death in mature erythrocytes: a model for investigating death effector pathways operating in the absence of mitochondria. *Cell Death Differ.* **8**, 1143–1156 (2001).

99. Lin, K.-H. *et al.* Enhancing Anticancer Effect of Gefitinib across the Blood–Brain Barrier Model Using Liposomes Modified with One α-Helical Cell-Penetrating Peptide or Glutathione and Tween 80. *Int. J. Mol. Sci.* **17**, (2016).

100. Puscas, I. *et al.* IVIVC Assessment of Two Mouse Brain Endothelial Cell Models for Drug Screening. *Pharmaceutics* **11**, 587 (2019).

101. Adriani, G., Ma, D., Pavesi, A., Kamm, R. D. & Goh, E. L. K. A 3D neurovascular microfluidic model consisting of neurons, astrocytes and cerebral endothelial cells as a blood–brain barrier. *Lab. Chip* **17**, 448–459 (2017).

102. Czupalla, C. J., Liebner, S. & Devraj, K. In vitro models of the blood-brain barrier. *Methods Mol. Biol. Clifton NJ* **1135**, 415–437 (2014).

103. Lippmann, E. S. *et al.* Derivation of blood-brain barrier endothelial cells from human pluripotent stem cells. *Nat. Biotechnol.* **30**, 783–791 (2012).

104. Rodriguez-Gaztelumendi, A., Alvehus, M., Andersson, T. & Jacobsson, S. O. P. Comparison of the effects of nicotine upon the transcellular electrical resistance and sucrose permeability of human ECV304/rat C6 co-cultures and human CaCo2 cells. *Toxicol. Lett.* **207**, 1–6 (2011).

105. Kapural, M. *et al.* Serum S-100β as a possible marker of blood–brain barrier disruption. *Brain Res.* **940**, 102–104 (2002).

106. Terrell-Hall, T. B., Ammer, A. G., Griffith, J. I. G. & Lockman, P. R. Permeability across a novel microfluidic blood-tumor barrier model. *Fluids Barriers CNS* **14**, 3 (2017).

107. Yeon, J. H. *et al.* Reliable permeability assay system in a microfluidic device mimicking cerebral vasculatures. *Biomed. Microdevices* **14**, 1141–1148 (2012).

108. Griep, L. M. *et al.* BBB on chip: microfluidic platform to mechanically and biochemically modulate blood-brain barrier function. *Biomed. Microdevices* **15**, 145–150 (2013).

109. Prabhakarpandian, B. *et al.* SyM-BBB: a microfluidic Blood Brain Barrier model. *Lab. Chip* **13**, 1093–1101 (2013).

110. Elbakary, B. & Badhan, R. K. S. A dynamic perfusion based blood-brain barrier model for cytotoxicity testing and drug permeation. *Sci. Rep.* **10**, 3788 (2020).

111. Brown, J. A. *et al.* Recreating blood-brain barrier physiology and structure on chip: A novel neurovascular microfluidic bioreactor. *Biomicrofluidics* **9**, 054124 (2015).

112. Xu, H. *et al.* A dynamic in vivo -like organotypic blood-brain barrier model to probe metastatic brain tumors. *Sci. Rep.* **6**, 36670 (2016).

113. Mehdipour, M. *et al.* Rejuvenation of three germ layers tissues by exchanging old blood plasma with saline-albumin. *Aging* vol. 12 8790–8819 https://www.aging-us.com/article/103418/text (2020).

114. Mehdipour, M. *et al.* Plasma dilution improves cognition and attenuates neuroinflammation in old mice. *GeroScience* **43**, 1–18 (2021).

115. Boada, M. *et al.* Plasma exchange for Alzheimer's disease Management by Albumin Replacement (AMBAR) trial: Study design and progress. *Alzheimers Dement. Transl. Res. Clin. Interv.* **5**, 61–69 (2019).

116. Reinhart, W. H. & Nagy, C. Albumin affects erythrocyte aggregation and sedimentation. *Eur. J. Clin. Invest.* **25**, 523–528 (1995).

117. Mark, K. S. & Davis, T. P. Cerebral microvascular changes in permeability and tight junctions induced by hypoxia-reoxygenation. *Am. J. Physiol. Heart Circ. Physiol.* **282**, H1485–H1494 (2002).

118. Hue, C. D., Cao, S., Dale Bass, C. R., Meaney, D. F. & Morrison, B. Repeated primary blast injury causes delayed recovery, but not additive disruption, in an in vitro blood-brain barrier model. *J. Neurotrauma* **31**, 951–960 (2014).

119. Haorah, J. *et al.* Ethanol-induced activation of myosin light chain kinase leads to dysfunction of tight junctions and blood-brain barrier compromise. *Alcohol. Clin. Exp. Res.* **29**, 999–1009 (2005).

120. Stone, N. L., England, T. J. & O'Sullivan, S. E. A Novel Transwell Blood Brain Barrier Model Using Primary Human Cells. *Front. Cell. Neurosci.* **13**, (2019).

121. Potter Claire M.F. *et al.* Role of Shear Stress in Endothelial Cell Morphology and Expression of Cyclooxygenase Isoforms. *Arterioscler. Thromb. Vasc. Biol.* **31**, 384–391 (2011).

122. Appelt-Menzel, A. *et al.* Establishment of a Human Blood-Brain Barrier Co-culture Model Mimicking the Neurovascular Unit Using Induced Pluri- and Multipotent Stem Cells. *Stem Cell Rep.* **8**, 894–906 (2017).

123. Brown, R. C., Morris, A. P. & O'Neil, R. G. TIGHT JUNCTION PROTEIN EXPRESSION AND BARRIER PROPERTIES OF IMMORTALIZED MOUSE BRAIN MICROVESSEL ENDOTHELIAL CELLS. *Brain Res.* **1130**, 17–30 (2007).

124. Yang, J. *et al.* A novel miR-200c/c-myc negative regulatory feedback loop is essential to the EMT process, CSC biology and drug sensitivity in nasopharyngeal cancer. *Exp. Cell Res.* **391**, 111817 (2020).

125. Wagner, H. J. *et al.* Characterization of the synthetic biology-inspired implementation of a materials-based positive feedback loop. *Data Brief* **19**, 665–677 (2018).

126. Weiner, O. D. *et al.* A PtdInsP3- and Rho GTPase-mediated positive feedback loop regulates neutrophil polarity. *Nat. Cell Biol.* **4**, 509–513 (2002).

127. Experimental validation of a predicted feedback loop in the multi-oscillator clock of Arabidopsis thaliana. *Mol. Syst. Biol.* **2**, 59 (2006).